Combined igneous and hydrothermal source for the Kiruna-type Bafq magnetite-apatite deposit in Central Iran; trace element and oxygen isotope studies of magnetite

Javad Mehdipour Ghazi[a,*], Chris Harris[b], Mohammad Rahgoshay[a], Mohssen Moazzen[c,d]

[a] Faculty of Earth Science, Shahid Beheshti University, Tehran, Iran
[b] Department of Geological Sciences, University of Cape Town, Cape Town, South Africa
[c] Department of Earth Sciences, University of Tabriz, 51666 Tabriz, Iran
[d] School of Earth & Environmental Sciences, University of Wollongong, Wollongong, NSW 2522, Australia

A B S T R A C T

The main deposits of the Bafq district (Choghart, Se Chahun and Chadormalou deposits) are magnetite-apatite ore bodies with Early Cambrian age, hosted by Early Cambrian volcano-sedimentary rocks, showing lava flow structure with miarolitic cavities and occasional brecciation. The texture and geochemistry (trace elements and O-isotope) of the studied magnetite crystals show three types of magnetite with different proportions in different parts of the district and the deposits. These are primary ignious magnetite and high-temperature hydrothermal magnetite in the massive parts of the deposits and foam-like magnetite in the veins or in the fractures of the massive part. The lack of zonation, high Ti/Fe ratios and $\delta^{18}O$ values (2‰ <) indicate that massive magnetites formed at high temperature condition, while foam-like magnetite recrystallized at lower temperature. Textures and Co, V, Ti, Al, and Pb contents are used to distinguish ignious magnetites from the high-temperature hydrothermal magnetites. Foam-like magnetites contain lower REE and has lower $\delta^{18}O$ values (2‰ >) than the massive magnetites.

The magmatic origin for the main part of the ores in the Bafq is more plausible. Contamination of the primary magmas of the Bafq magmatic rocks with crustal phosphorus and evaporate units was the major agent for triggering iron-rich melt immiscibility from the original magma. Concentration of volatiles in the iron-rich melt involving in crystallization of the primary magnetite and nucleation of the aqueous fluid bubbles on magnetite surfaces led to ascending the buoyant fluid bubble-magnetite aggregates. This caused continuation of the magmatic magnetite microlites growth from the iron-rich magmatic-hydrothermal fluid and formed high-temperature hydrothermal magnetite. Formation of hypersaline fluid due to crystallization of iron-rich melt at shallow depth led to crystallization of titanite (and Th-U-REE-bearing minerals) and sodic-calcic alteration related to magnetite mineralization. Microscopic evidence (replacement of magnetite by hematite and filling of fractures of thorite by magnetite) show that degassing continued at shallow depth, which led to re-crystallization of the primary magnetites and formation of the foam-like magnetites.

1. Introduction

The main iron (magnetite-apatite) deposits of Iran are located in the Posht-e-Badam Micro Block of Central Iran, known as Bafq district. It contains significant bodies of magnetite mineralization as reflected by 34 major magnetic targets. The genetic model for the Fe deposits in this district is a subject of a long-standing debate. Förster and Jafarzadeh (1994) suggested a magmatic model involving immiscible liquids model for the formation of deposits of the Bafq district. Daliran et al. (1999) and Aftabi et al. (2009) recognised characteristics of sedimentary-exhalative origin for some deposits of the Bafq district and, therefore, argued that some of the iron deposits are sedimentary-exhalative type. Daliran (2002) proposed that hydrothermal fluids had played a significant role in development of the deposits. For the Choghart deposit, Moore and Modabberi (2003) proposed that the separation of an iron oxide melt and the ensuing hydrothermal processes dominated by alkali metasomatism were both involved to different degrees in the formation of Choghart and other similar deposits in Central Iran. According to a
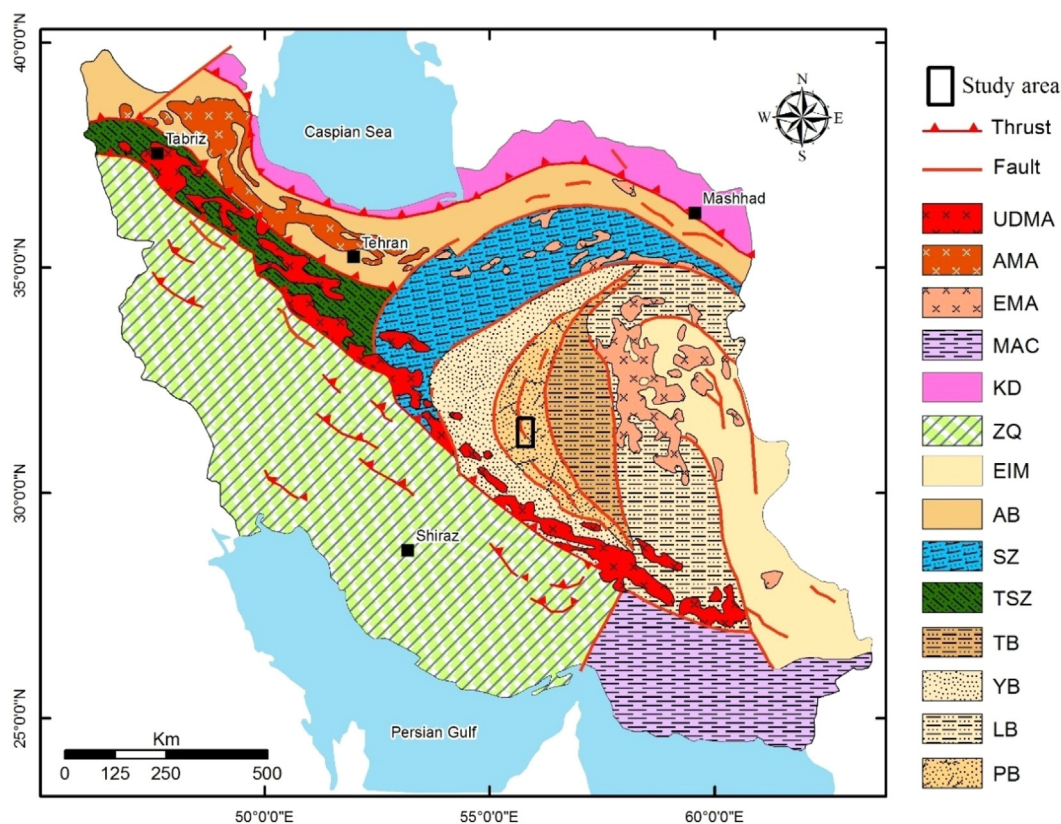
Fig. 1. Simplified geological map of Iran from Aghanabati (2006) and location of the study area. UDMA: Urumieh-Dokhtar Magmatic Arc, AMA: Alborz magmatic belt, EMA: East Iran magmatic arc, MAC: Makran accretionary complex, KD: Kopeh Dagh zone, LB: Lut block, SZ: Sabzevar zone, ZQ: Zagros orogeny, AB: Alborz belt, EIM: East Iran, TSZ: Tabriz-Saveh zone, TB: Tabas block, Yb: Yazd block, LB; Lut block, PB: Posht-e-Badam block.

study of the Bafq district by Torab and Lehmann (2007), the magnetite-apatite deposits are probably related to large-scale brine circulation induced by felsic magmatism during the Cambrian. Jami et al. (2007) presented evidence from the Esfordi deposit indicating that an evolving hydrothermal system associated with submarine magmatic activity might have been responsible for ore generation. Daliran et al. (2010) and Heidarian et al. (2018) proposed a model of large-scale, multi-stage metasomatism associated with Early Cambrian magmatism. Mokhtari (2013) proposed a magmatic model for iron oxide-apatite (IOA) deposits in the Bafq district. Taghipour et al. (2013) argued that mixing of magmatic and non-magmatic fluids caused iron oxide mineralization and hydrothermal alteration in the Choghart deposit. However, in the latest paper by Taghipour et al. (2015) they compared the Bafq iron oxide-apatite deposits with other Kiruna-type iron oxide-apatite deposits and suggested that they formed from highly differentiated volcanic magmas which interacted with both magmatic and externally derived fluids shortly after crystallization and during cooling. Mohseni and Aftabi (2015) advanced the view that the Central Iranian iron deposits were formed as glaciogenic banded iron formation (Rapitan BIF type). Heidarian et al. (2017) proposed two stages of formation for Chadormalou deposits; the first stage was responsible for formation of massive-type ore from magmatic derived fluids and, in the second, evolving fluid from magmatic to surficial brine-rich fluid formed vein-type ore. In short, the recent findings mostly consider the deposits in the Bafq district to be of the Kiruna-type. However, the details of the origin and mechanism of formation are controversial, as are possible differences between deposits of the district.

Kiruna-type iron oxide-apatite deposits are generally associated with volcanic and intrusive rocks and occur world-wide (Hitzman et al., 1992; Hitzman, 2000). They are dominated by sulfide-poor mineral assemblages of low-Ti magnetite, fluorapatite and actinolite (Hildebrand, 1986; Nyström and Henríquez, 1994). Kiruna-type

deposits, named after the Kiruna deposit in Sweden (Geijer, 1931), comprise low-Ti (< 1 wt%) magnetite ± trace titanite, and apatite is generally less abundant compared to nelsonites (Knipping et al., 2015). Mineville deposit in New York, as a Kiruna-type deposit, contains as much as 50% apatite (Foose and McLelland, 1995) and El Laco deposit in Chile contains only accessory amounts of apatite (Nyström and Henríquez, 1994). Magnetite and apatite in Kiruna-type deposits reflect the conditions and evolution of ore generation and have been used as petrogenetic indicators (e.g. Frietsch and Perdahl, 1995). Magnetite forms under a wide variety of conditions, crystallizing at high temperature from silicate and sulfide melts or precipitating at lower temperatures from hydrothermal fluids (e.g. Simon et al., 2004; Dare et al., 2014; Knipping et al., 2015). Due to a large number of minor and trace elements substitutions into magnetite, these different conditions lead to distinctive trace element signatures in magnetite (Dare et al., 2014). Therefore, geochemical data of this mineral along with oxygen isotope data could help to understand origin and evolution of these deposits, and Kiruna-type deposits in general.

Although the Choghart, Se Chahun, and Chadormalou magnetite-apatite deposits are the largest and important deposits of the Bafq district and have attracted a substantial number of studies, the genetic relationship is still poorly understood and the magmatic or hydrothermal origin of the magnetite–apatite deposits in this region is still debated. The mechanism of ore fluid/melt generation and migration is also controversial. In this paper, we report the mineral trace elements (including REE) geochemistry and O-isotopic composition of magnetite from the Choghart, Se Chahun and Chadormalou magnetite-apatite deposits and investigate the possible differences. The data presented in this paper are a prerequisite for constraining the genesis of these deposits, and are used to improve the metallogenic model of the Posht-e-Badam micro block of Iran.

2. Geology

2.1. Regional geology of the Bafq district

The Iranian Plateau is a tectonically active region within the Alpine-Himalayan orogenic belt and contains a number of continental fragments bounded by major faults that have been welded together along suture zones of oceanic character. The Central Iranian Micro-continent (CIM, Takin, 1972) comprises a terrane delimited by the Sistan, Nain-Baft and Makran ophiolitic belts, plus the Darouneh Fault and the Sabzevar ophiolites (Şengör, 1990). The CIM is divided into four major blocks (Yazd, Posht-e-Badam, Tabas and Lut), separated by generally N-S, right-lateral, strike-slip faults, concaved to the east (Aghanabati, 2006). The Micro-Block of Posht-e-Badam is located between the western Yazd Block and the Tabas Block that, together with the Lut Block further to the East, constitute the crustal domain of the Central Iranian Terrane (Fig. 1). The micro-block is a relatively narrow metallogenic/tectonic province of Neoproterozoic age, with the most important iron ore resources of Iran located between Bafq City in the south and Posht-e-Badam village in the north. The arcuate block is dominated by fault structures.

Geological units of the Bafq district can be temporally divided into Neoproterozic, Cambrian and younger sequences. The Bafq district comprises a basement of Neoproterozoic metamorphic rocks that has been interpreted as a series of horst and grabens, Early Cambrian diorites to tonalities (Narigan-Zarigan granitoids), an un-metamorphosed Early Cambrian volcano-sedimentary unit with minor evaporites (Rizo Formation) and individual volcanic rocks (Fig. 2). The Neoproterozoic and Cambrian units are covered by a series of Palaeozoic to Quaternary sedimentary strata with various rock types.

This micro-block is the most important iron metallogenic province in the region, with world class iron deposits. They are hosted by an un-metamorphosed Early Cambrian volcano-sedimentary unit (Rizo Formation) and subvolcanic intrusions. There are several non-ferrous ore bodies containing Pb-Zn, Mn, U and Mo.

2.2. Geology of iron deposits

There are three important magnetite-apatite deposits in the Posht-e-Badam micro block (Bafq district) that are oldest and high-grade mines of Iran. The Choghart iron deposit is located 12 km northeast of Bafq, and is the most southerly deposit of the three. The Se Chahun deposit with two separate ore zones (anomalies X and XI) is located between two other deposits. The Chadormalou deposit is located about 80 km north of Bafq at the north and is the largest deposit in the Posht-e-Badam block. The simplified cross-sections of these deposits are presented in Fig. 4.

Unfortunately, geological and structural features related to iron mineralization in the Bafq district, especially in the mines, are lost due to extensive mining and extraction activities, or are covered by waste depots and expansion of infrastructures. The only visible features around the studied mines include the following. The ore body is characterized by miarolitic cavities (tubes) and amygdaloidal structures in massive ores, in which some parts are filled by secondly hydrothermal minerals such as hematite, calcite and chlorite (Fig. 4A). In addition, magmatic flow structures are evident in some parts. The orebody and
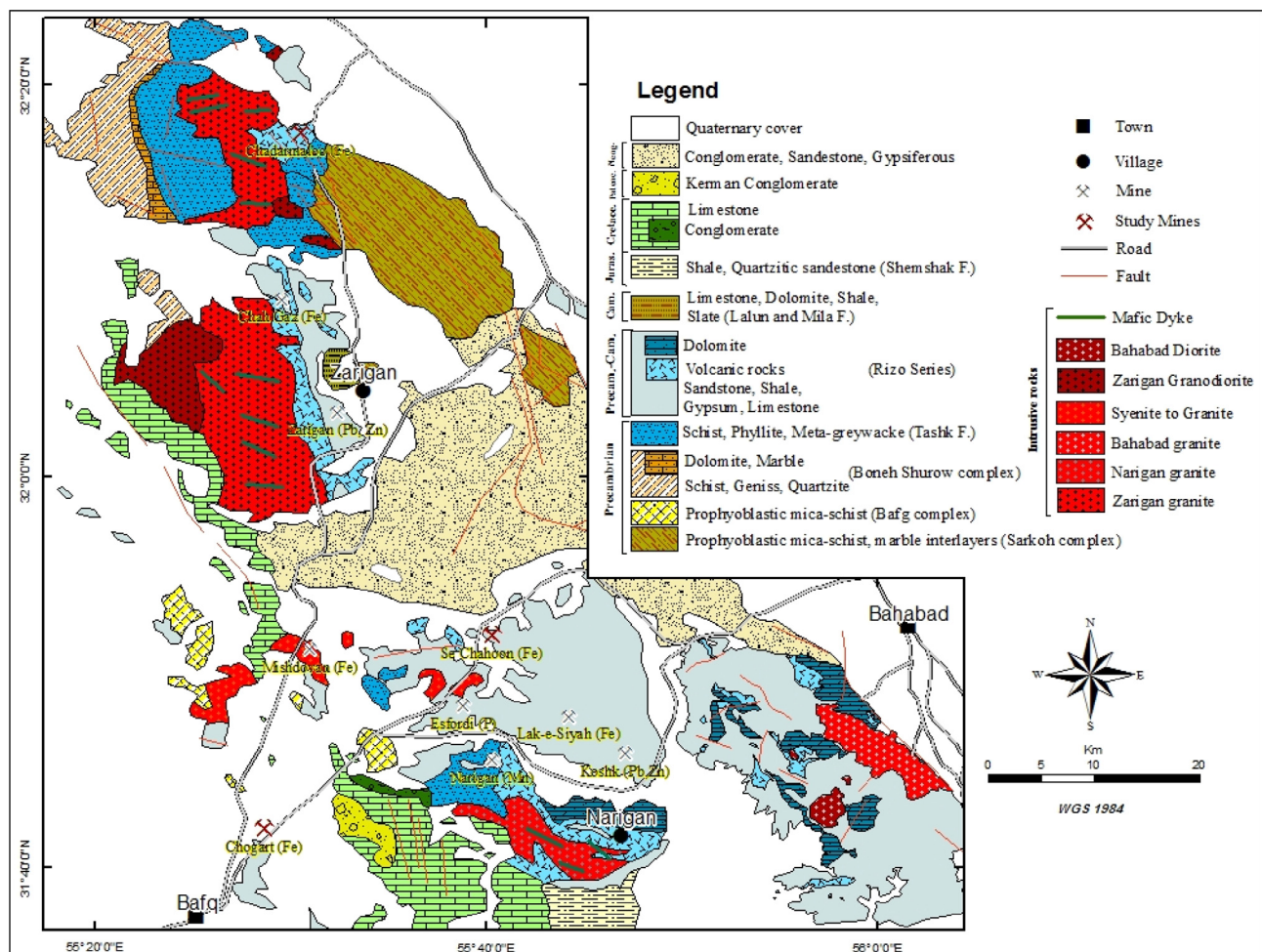

Fig. 2. Simplified geological map of the Bafq region showing the location of magnetite-apatite deposits (modified after Haghipour and Pelissier, 1977).
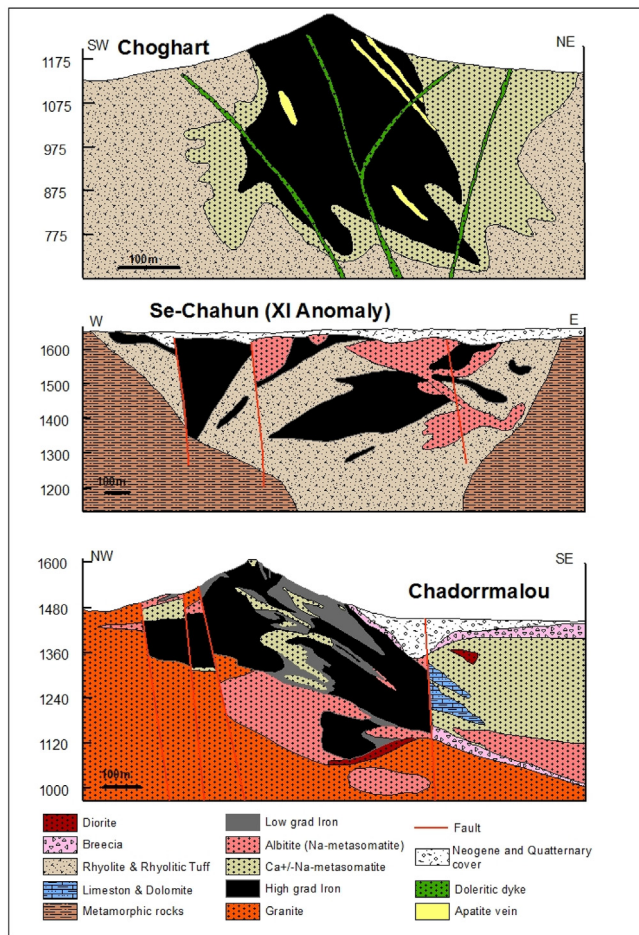
Fig. 3. Simplified cross-sections of the Choghart, Se Chahun and Chadormalou deposits (Modified from Förster and Jafarzadeh, 1994).

country rocks are cut by several mafic dikes (Fig. 4B, C).

Geology of the ore deposits of the Bafq district has been dealt with by many authors. Their geological characteristics are summarized below separately.

2.2.1. Choghart deposit

Country rocks of the Choghart ore body are metasomatized and brecciated volcanic rocks and dolomite, belonging to the Early Cambrian Rizo Formation (Fig. 3A). The ore body has been explored to a depth of about 600 m and is in form of roughly vertical, discordant and pipe shaped body. The ore body appears to inter-finger with wall-rock at the bottom and the rims. Fig. 4 shows the schematic geological cross section of the deposit.

All rocks in the ore district, even mafic dikes, suffered varying degree of hydrothermal alteration and display extensive mineralogical, textural and compositional diversity. The massive magnetite constitutes the lower part of the ore body. Accessory minerals include apatite, pyrite, actinolite-tremolite, calcite, talc, titanite, pyroxene, rutile and quartz. The oxidation zone reaches 150 m depth and varies from incipient martitization (changing of primary oxides to geothite and hematite) to complete replacement of magnetite by martite near the surface. Hematite is the second most ubiquitous mineral after magnetite. Although some primary hematite is found in the drill cores, most of the hematite is secondary in origin. Some goethite and hydrous iron oxides occur near the surface but disappear rapidly with depth. Fine- and coarse-grained apatite occurs in varying proportions with magnetite.

At least two generations of apatite are discernible (Moore and Modabberi, 2003). The first, which is contemporaneous with the main phase of iron oxide formation, displays euhedral crystals ranging in size from a few millimetres to a few centimetres in diameter. It is intimately intergrown with magnetite. Their generation may correlate with presented age for ore formation, 515 ± 21 and 529 ± 21 Ma (monazite Th-U- total Pb method, Torab and Lehmann, 2007). The second generation occurs as subhedral to anhedral crystals in lenses, dykes, and veinlets of varying size and thickness, which cut the magnetite-apatite ore. Their age could be correlated with reported age by Stosch et al. (2011) for apatite of Choghart (440 Ma). Pyrite and quartz are distributed quite evenly in the orebody and sometimes formed veins (Fig. 4D), either as solid inclusions in primary magnetite grains or as well-developed crystals in the orebody and the adjacent country rocks (Khoshnoodi et al., 2017). In Choghart ore deposit, two generations of thorite are formed. The first generation is presented as disperse phase during sodic-calcic alteration related to magnetite ore body and the second generation occurs as veinlet, disseminated and inclusion in other minerals such as albite and clinopyroxene, associated with Th-REE mineralization (Khoshnoodi et al., 2017). It seems that some
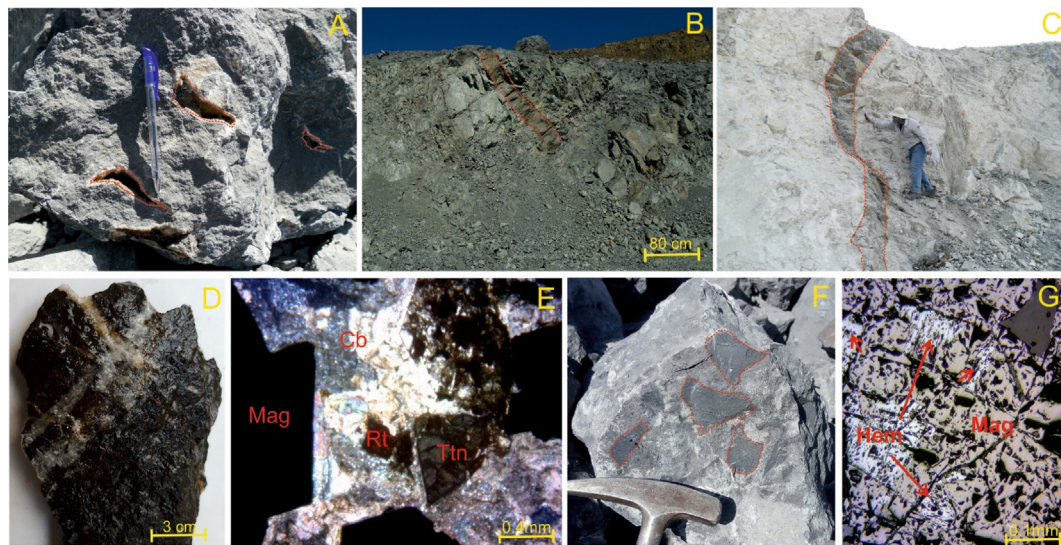
Fig. 4. (A) Field photo of miarolitic cavities in ore body that were filled by calcite, (B) metasomatic mafic dike within ore body, (C) metasomatic mafic dike within altered volcanic rock, (D) vein of quartz and pyrite in the low grade ore, (E) microscopic photo of titanite and rutile in the carbonate vein in the ore body, (F) fragments of iron ore in the brecciation zone, (G) microscopic photo of replacement of magnetite by hematite.

titanites are primary and occur as individual minerals between magnetites and some are secondary, formed during hydrothermal process since they occur in the carbonate assemblage and are changed to rutile in some parts (Fig. 4E). The occurrence of magnetite as a fracture filling phase in thorite is reported by Khoshnoodi et al. (2017). At least two phases of sodic-calcic alteration occurred in this deposit; the first phase is related to iron mineralization and the second is associated with Th-REE mineralization. Pyroxene of the first phase is diopside (Sadeghi Davati et al., 2008) and pyroxene of the second phase has mostly augite composition (Khoshnoodi et al., 2017).

2.2.2. Se Chahun deposit

Ore occurrences in this deposit consist of some tabular- to lens-shaped ore bodies. They host are altered rhyolitic tuff, shallow-water sandstone, dolomitic limestone and shale of Early Cambrian Rizo Formation (Fig. 3B). The U-Pb age of coarse REE-rich fluorapatite is reported to be 510 ± 8 Ma and 525 ± 7 Ma from Se-Chahun deposit by Bonyadi et al. (2011).

At the eastern part of the Anomaly X, a persistent jaspilite horizon is present, accompanied by iron mineralization, which occurs 200 m stratigraphically below the jaspilite horizon. The Anomaly XI occurs 3 km northeast of the Anomaly X. The Anomaly XI ore bodies contain 89% of the ore reserves (average grade of 36–37% Fe), although the massive (with minor banded) magnetite-actinolite ore in the Anomaly X has a higher grade (up to 67 wt% Fe; Förster and Jafarzadeh, 1994).

Brecciation is variably developed in this mineralization (Fig. 4F), with smaller fragment sizes in the apatite zones (up to 2 mm) versus the magnetite zones (up to 7 mm diameter). Brecciated zone mainly includes K-feldspar, biotite, actinolite, titanite, ilmenite, sulphide minerals and rutile (Bonyadi et al., 2011). A relict, variably brecciated sedimentary banding can be seen in other parts of this anomaly. The host rocks and the ore bodies are crosscut by E–W-trending normal faults. In addition, late E–W oriented mafic dikes locally cut the ore bodies and the alteration zones.

Back-scattered electron image and element mapping studies of Se-Chahun magnetite by Bonyadi et al. (2011) show two types of magnetite in this deposit; primary magnetite 200 μm diameter in average and euhedral, and secondary anhedral magnetite with 100 μm diameter in average. All primary magnetite crystals are Al-depleted and show speckled ilmenite exsolution texture at crystal rims (Bonyadi et al., 2011).

Accessory minerals in this deposit include apatite, actinolite-tremolite, thorite, calcite, pyrite, epidote, titanite, huttonite, quartz and albite. Generally, the ore in the Anomaly XI has lower phosphorus content than that of the Anomaly X. Titanite in this deposit not only occurs in the breccia matrix with strongly tendency to rutile but occurs as a lining to inter magnetite carbonate matrix in the unbrecciated zones.

2.2.3. Chadormalou deposit

The ore body in this deposit is in two parts with different forms. The northern ore body is in form of an upright cylinder with several horizontal extensions, interpreted as a magnetite-filled vent, more than 600 m deep (Fig. 3C). The southern ore body is a flat-lying lens, interpreted as magnetite lava flow or sill, emitted from the vent in a ring graben toward south-southwest (Förster and Jafarzadeh, 1994). The host rocks of the ore bodies are Precambrian metamorphic rocks, and Early Cambrian hydrothermally altered volcanic rocks (predominantly rhyolite), with intercalations of siliceous dolomite and pyroclastic breccia, belonging to the Rizo Formation and in association with Early Cambrian Chadormalou granitoid. All rock types in the ore district are cut by mafic dikes. The massive ore body is cut by veins of albitite in some parts. The rhyolite host rocks are also strongly altered.

The oxidation zone reaches down to 150 m depth, and ranges from incipient martitization to complete replacement of magnetite by martite and secondary formation of hematite. Exsolution textures in magnetite

are rare (Förster and Jafarzadeh, 1994). Study of SEM backscattered electron images by Heidarian et al. (2016) revealed three main magnetite generations: magnetite with porous and dark appearance (that are primary magnetite) variably replaced by a lighter magnetite (secondary magnetite). The porous appearance of the former magnetite developed through dissolution processes (Heidarian et al., 2017). The primary magnetite displays sharp and irregular contact with secondary magnetite and some primary magnetite show 120 triple junctions with each other (Heidarian et al., 2017). Alteration is locally developed in the different magnetite crystals, distinguished by replacement of primary magnetite by hematite (Fig. 4G). Dolomite, quartz, calcite, talc, chlorite, actinolite, albite and phlogopite occur within the coarse-grained magnetite-apatite ore. Cracks in large apatite crystals are filled by carbonate.

2.3. Characteristics of magmatic host rocks

The contemporary magmatic rocks in the Bafq district with iron deposits include volcanic rocks of the Rizo Formation and shallow intrusions. The volcanic rocks of Rizo Formation are trachyte, andesite, rhyolite and tuff. These volcanic rocks can be attributed to submarine volcanism as they show sequential facie with dolomitic rocks. They show calc-alkaline to alkaline nature and are generated in a supra-subduction zone (Ramezani and Tucker, 2003; Heidarian et al., 2017; Khoshnoodi et al., 2017; Eslamizadeh, 2017). No geochemical signatures of magma mixing have been reported for evolution of the parental magmas of these rocks. However, they show crustal contamination (e.g. Eslamizadeh, 2017). The rhyolite and dacite-porphyry samples from this unit produced concordant U/Pb ages of 529.7 and 528 Ma, respectively (Ramezani and Tucker, 2003).

The shallow intrusions have granite, syenite, granodiorite and diorite compositions with mostly porphyritic to granular textures (Fig. 5). They show mostly I-type characteristics (e.g. Ramezani and Tucker, 2003; Jami, 2005). These intrusions are known as Narigan, Zarigan, Chah Choleh and Esfordi granites in the Bafq district. Geochronology data of Zarigan leucogranite show Early Cambrian age, (525 ± 7 Ma, Ramezani and Tucker, 2003). Geochemical data of these rocks are similar to volcanic rocks of the Rizo Formation (e.g. Ramezani and Tucker, 2003; Jami, 2005; Torab, 2008). It seems that volcanic and intrusive rocks are co-magmatic. According to Ramezani and Tucker (2003) the Early Cambrian granite-tonalite plutons, as well as the volcanic rhyolite-dacite associations (CVSU), demonstrably originated in an active margin environment and do not show alkaline affinities attributable to intra-plate magmatism. The late-stage, massive trondhjemite intrusions of the Saghand area provide further evidence for the Early Cambrian subduction of young oceanic crust. In summary, geologic, geochronologic and geochemical observations in Central Iran are consistent with a major episode of latest Neoproterozoic to Early Cambrian orogenic activity in an active continental-margin environment. The upwelling and emplacement of the generated magma from partial melting of the subduction-modified mantle in the lower crust was evolved by crustal contamination and crystal fractionation. Ascending magma to shallow magma chambers or eruption in the different time intervals show little diversities in these rocks due to different ratios of crustal contamination and fractionation.

2.4. Alteration

Sodic alteration is widespread in the Bafq district. It has affected all rocks of the area. The sodic alteration resulted in the formation of fine- to coarse-grained albite with commonly chessboard texture and pink colour (Fig. 6A; Heidarian et al., 2017). Th-REE mineralization occurred in the sodic alteration zones (Khoshnoodi et al., 2017). The U-Pb age of sodic alteration in the Se-Chahun deposit is 525 ± 7 Ma (Bonyadi et al., 2011). Some studies (e.g. Torab, 2008; Heidarian et al., 2017) consider evaporate origin for sodic metasomatism in the area.
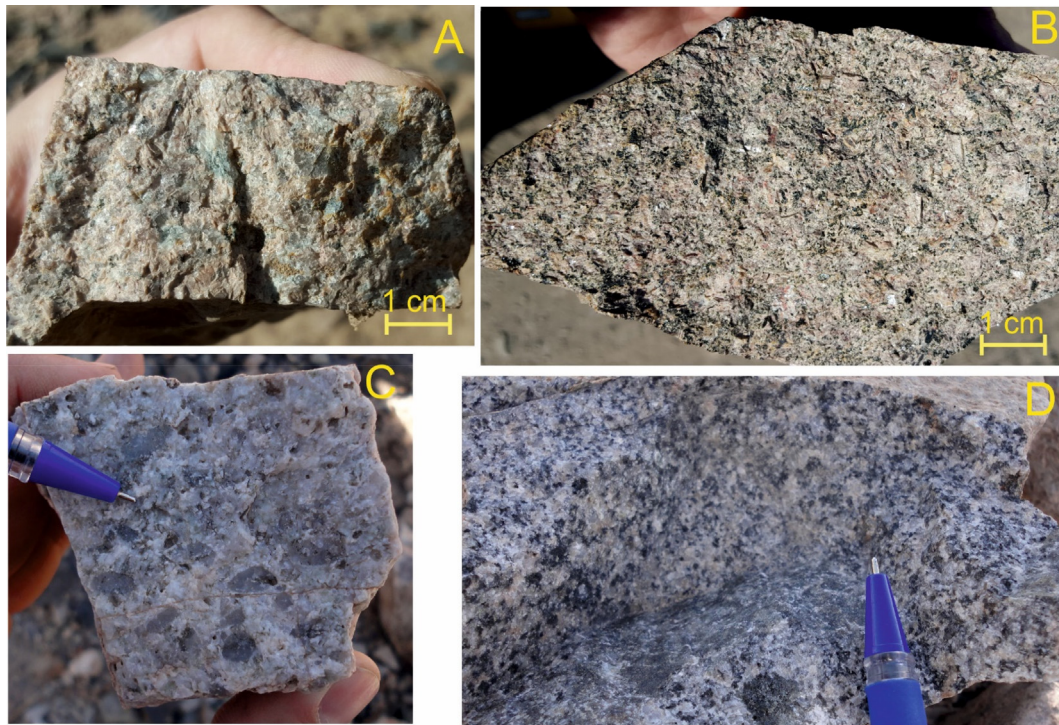
Fig. 5. Hand samples of igneous rocks from the Bafq district. (A) granular granite, (B) micro granular syenite, (C) porphyritic leucogranite, and (D) granular granodiorite.

Sodic alteration occurs rather distal to the ore bodies; the alteration is increasingly replaced by calcic alteration toward the ore bodies (Heidarian et al., 2017). In the Se-Chahun deposit, the host rocks strongly altered by both early sodic (chessboard albite) and younger pervasive sodic–calcic alteration (amphibole–albite–magnetite–calcite–epidote–quartz–titanite–allanite) that is associated with magnetite–apatite mineralization (Bonyadi et al., 2011). Two phases of sodic-calcic alteration occurred in the Bafq district. The first phase is related to
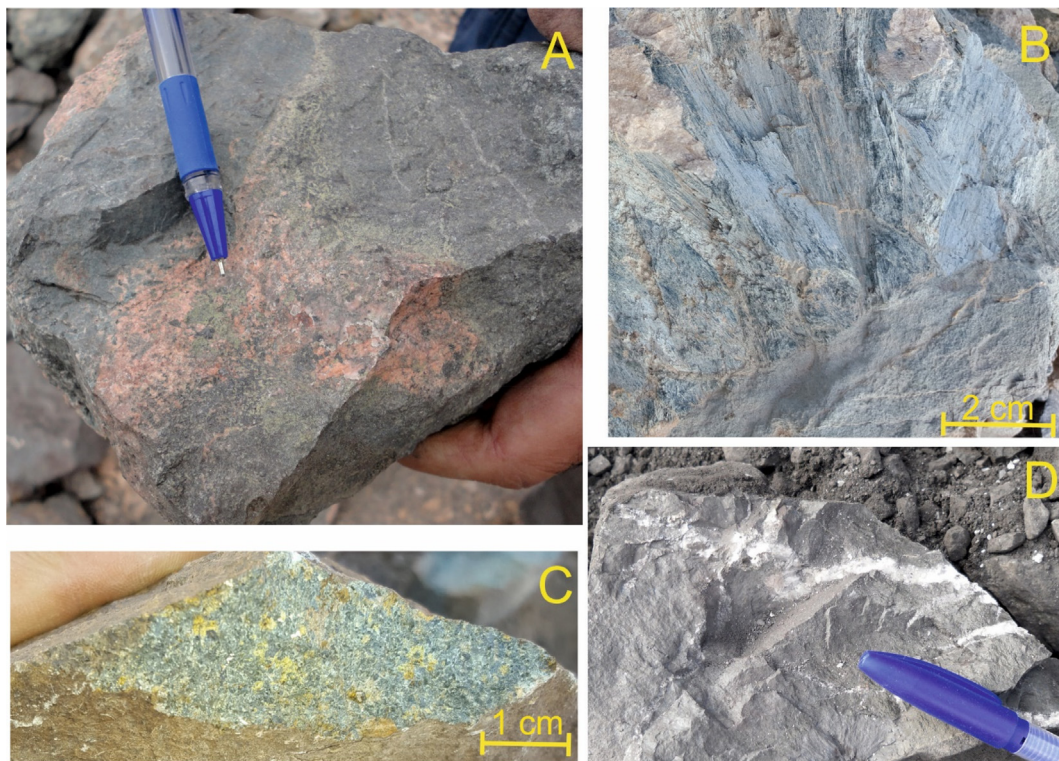
Fig. 6. Hand samples of different altered rocks in the Bafq district. (A) pink albite (sodic alteration) within ore body, (B) green mega actinolite assemblage (calcic alteration), (C) sericitic altered rock, and (D) calcite veinlets in the ore body. (For interpretation of the references to color in this figure legend, the reader is referred to the web version of this article.)

Table 1

LA-ICP-MS analysis (ppm) of magnetite from different magnetites (P(I).Mag.: primary igneous magnetite, S(H).Mag.: surrounding High T-hydrothermal magnetite, F.Mag.: Foam-like magnetite) of the Bafq deposits (PZ01: magnetite from lave flow structure ore near Se Chahun deposit, SN01: magnetite from X- anomaly of Se Chahun mine bottom levels, SN24: magnetite from XI- anomaly of Se Chahun mine bottom levels, S01: magnetite from surficial pack of ore near Se Chahun, MCT8: magnetite from Choghart mine bottom levels, MCL9: magnetite from Chadormalou mine bottom levels).

|	PZ01_1	PZ01_2	PZ01_3	PZ01_5	PZ01_6	PZ01_7	PZ01_8	PZ01_9	PZ01_10	MCL9_4	SN01_1	SN01_2	SN01_3
	P(I). Mag.	P(I). Mag.	P(I). Mag.	P(I). Mag.	P(I). Mag.	P(I). Mag.	P(I). Mag.	P(I). Mag.	P(I). Mag.	P(I). Mag.	P(I). Mag.	P(I). Mag.	P(I). Mag.
Mg	1190	1089	1316	1900	793	605	374	814	459	1045	326	527	401
Al	1452	1259	1078	1352	908	1029	916	799	476	267	890	1340	1229
P	9.5	38.1	43.1	24.3				6	27.6		3.7		
Ca	468	610	949	820	168	196	141	208	130	339	222	211	201
Ti	7420	6310	5530	5910	5470	4970	7220	6550	6040	4870	10,740	10,540	8850
V	2907	2890	2936	2862	2876	2870	2984	2956	2966	2425	2922	2908	2960
Cr	0.82	1.21	1.25	1		1.75	1.68	1.46	1.01		5.56	6.87	9.96
Co	84.42	83.4	88.1	85.4	80.8	76.5	78.2	82.8	79.8	49.12	90.2	90.6	90.6
Ni	386.6	399.1	396.7	411.4	403.7	399.1	370.2	352.7	344.9	182.9	251.4	258	267.9
Y	2.36	6.18	4.88	4.16	1.77	11.76	0.561	2.33	2.636	1.359	0.464	0.449	0.475
La	0.74	6.36	8.27	4.4	0.549	2.06	0.13	1.166	3.93	2.92	0.616	0.395	0.657
Ce	2.71	18.49	27.37	15.45	1.99	8.64	0.96	3.01	6.48	8.4	1.141	0.886	1.403
Pr	0.396	1.732	2.43	1.441	0.301	1.383	0.0732	0.36	0.611	1.029	0.1233	0.116	0.159
Nd	1.71	5.86	7.84	4.87	1.3	6.42	0.31	1.465	2.04	3.16	0.41	0.437	0.62
Sm	0.394	0.968	1.063	0.788	0.288	1.69	0.08	0.3	0.306	0.486	0.097	0.094	0.121
Eu	0.0493	0.0995	0.0964	0.0804	0.0328	0.197	0.0101		0.0326	0.042	0.0131	0.0204	0.024
Gd	0.421	0.931	0.813	0.652	0.291	1.927	0.087		0.326	0.331	0.095	0.088	0.131
Tb	0.0597	0.1445	0.1091	0.0928	0.0393	0.269	0.0137	0.06	0.0595	0.0449	0.0154	0.0177	0.0208
Dy	0.345	0.964	0.713	0.632	0.259	1.743	0.081	0.355	0.425	0.22	0.0853	0.0859	0.11
Ho	0.0688	0.2021	0.1741	0.137	0.0509	0.351	0.0206	0.0737	0.093	0.0524	0.0201	0.0254	0.0296
Er	0.219	0.706	0.614	0.463	0.151	1.109	0.0609	0.245	0.295	0.1314	0.0495	0.0654	0.065
Tm	0.0319	0.1005	0.0911	0.0649	0.0187	0.134	0.0085	0.0373	0.0453	0.0214	0.0106	0.0115	0.0109
Yb	0.236	0.646	0.577	0.507	0.134	0.992	0.062	0.251	0.257	0.15	0.062	0.073	0.065
Lu	0.0393	0.0838	0.0761	0.0678	0.0249	0.155	0.0102	0.037	0.0364	0.0268	0.0143	0.0125	0.0121
Pb	0.93	0.87	1.79	3.44	0.95	1.75	0.531	1.12	0.342	0.0732	4.89	3.242	8.67
EREE	7.42	37.2874	50.2368	29.6459	5.4296	27.07	1.9072	7.726	14.9368	17.0149	2.7526	2.3278	3.4284

	SN01_4	SN01_5	SN01_6	SN01_7	SN01_8	SN01_9	SN01_10	SN01_11	SN01_12	SN21_1	SN21_4	SN21_6	SN21_2
	P(I). Mag.	P(I). Mag.	P(I). Mag.	P(I). Mag.	P(I). Mag.	P(I). Mag.	P(I). Mag.	P(I). Mag.	P(I). Mag.	P(I). Mag.	P(I). Mag.	P(I). Mag.	P(I). Mag.
Mg	950	155.8	221	261	98.9	253	512	1113	545	347	158	67.1	128
Al	1970	1973	2159	560	2340	836	2093	2447	863	523	213	449	254
P													
Ca	68	50	88	1400	91	134	3860	111	275	1550	101		280
Ti	11,710	12,410	12,760	6960	10,340	7820	11,970	12,260	9600	3450	3190	8810	2750
V	2847	2807	2825	2776	2848	2866	2875	2838	2835	3380	3400	3549	3437
Cr	2.08	1.05		1.36	0.59	1.16	2.94	2.76	1.45			0.73	
Co	93.7	91.8	92.15	87.4	100	87.5	97.3	93.3	91.5	32.82	31.11	30.4	31.71
Ni	271.2	273	274.7	255.2	272.5	269.4	281.7	277.2	270.1	239.4	241.5	247.9	235.4
Y	0.28	0.1027	0.0866	0.34	0.2049	0.486	0.37	0.629	0.82	4.2	0.0649	0.121	0.635
La	0.282	0.1233	0.0864	0.517	0.414	0.957	0.521	0.563	1.13	2.99		0.0183	4.17
Ce	0.575	0.2429	0.165	1.099	0.783	1.849	0.994	1.06	2.14	3.7	0.0104	0.0303	3.31
Pr	0.0502	0.0226	0.0157	0.1315	0.1002	0.1953	0.0954	0.1045	0.218	0.518		0.0031	0.366
Nd	0.166	0.0673	0.0425	0.446	0.356	0.635	0.332	0.353	0.611	2.03			1.13
Sm	0.0285			0.093	0.086	0.117	0.071	0.0723	0.125	0.63			0.18
Eu				0.0166	0.0179	0.0204	0.0096	0.0096	0.0207	0.199			0.0394
Gd	0.037			0.096	0.082	0.114	0.073	0.0612	0.128	0.73		0.0106	0.195
Tb	0.0071	0.00237		0.0154	0.0141	0.0166	0.0113	0.0158	0.0254	0.138	0.00118	0.00199	0.0245
Dy	0.0368	0.0152	0.0109	0.0752	0.0512	0.0922	0.0545	0.0792	0.133	0.96	0.011	0.017	0.123
Ho	0.0107	0.0033	0.00251	0.0193	0.0107	0.0231	0.0139	0.0253	0.0322	0.18	0.00208	0.0053	0.0246
Er	0.0315	0.0082	0.0086	0.047	0.0217	0.0502	0.0376	0.0724	0.094	0.56		0.0216	0.08
Tm	0.005	0.00193	0.00107	0.0064	0.00434	0.0076	0.0066	0.0135		0.072	0.00248	0.00387	0.0123
Yb	0.0328	0.0086		0.0424		0.0513	0.042	0.09	0.107	0.46	0.0151	0.0297	0.073
Lu	0.0061			0.0059	0.00293	0.0064	0.0073	0.0144	0.0175	0.052	0.005	0.0062	
Pb	0.233	0.095	0.317	5.58	4.17	8.14	0.357	0.1	4.48		0.282	0.606	1.68
EREE	1.2687	0.4957	0.33268	2.6107	1.94407	4.1351	2.2692	2.5342	4.7818	13.219	0.04724	0.14796	9.7278

	SN21_3	SN21_5	MCT8_7	MCT8_5	MCT8_1	PZ01_4	MCT8_3	MCT8_8	MCT8_4	MCL9_5	MCL9_6	MCL9_7	MCL9_8
	P(I). Mag.	P(I). Mag.	P(I). Mag.	P(I). Mag.	P(I). Mag.	S(H). Mag.	S(H). Mag.	S(H). Mag.	S(H). Mag.	S(H). Mag.	S(H). Mag.	S(H). Mag.	S(H). Mag.
Mg	138	46.1	2920	1708	1854	771	2551	2079	1771	577	95.1	77.7	278
Al	224	102.3	1801	1805	1752	982	1887	1744	1811	120.2	103	95.4	90.9
P					14.5	4.7							
Ca	318	60		54	187	421	140	62		66			100
Ti	2380	1852	15,600	3990	3530	3640	4020	5420	5710	4730	3950	3615	3620
V	3439	3335	2477	2506	2467	2944	2468	2503	2486	2397	2243	2256	2208
Cr	1.18	21.98		1.72		1.33			2.84		0.81		

(continued on next page)

Table 1 (*continued*)

	SN21_3	SN21_5	MCT8_7	MCT8_5	MCT8_1	PZ01_4	MCT8_3	MCT8_8	MCT8_4	MCL9_5	MCL9_6	MCL9_7	MCL9_8
	P(I). Mag.	P(I). Mag.	P(I). Mag.	P(I). Mag.	P(I). Mag.	S(H). Mag.	S(H). Mag.	S(H). Mag.	S(H). Mag.	S(H). Mag.	S(H). Mag.	S(H). Mag.	S(H). Mag.
Co	32.25	30.99	86.59	77.01	48.17	85.46	69.79	83.42	76.76	49.14	48.62	48.59	49.03
Ni	235.4	234.5	421.8	418.8	423.5	415	427.3	416.1	418.3	178.6	176.3	176.2	178.2
Y	0.49	0.0893	0.0799	0.0189	0.415	2.33	0.341	0.0616	0.0337	0.666	0.1049	0.0496	0.4
La	0.7	0.026	0.1435	0.139	0.667	1.772	0.599	0.135	0.289	0.472	0.0863	0.0334	0.349
Ce	1.74	0.067	0.38	0.119	2.666	5.5	2.201	0.333	0.377	2.148	0.1884	0.0697	1.096
Pr	0.222	0.0091	0.0412	0.0125	0.295	0.589	0.257	0.0351	0.0335	0.233	0.0185	0.0086	0.1321
Nd	0.8	0.0288	0.111	0.026	1.016	2.19	0.906	0.118	0.098	0.765	0.065	0.0268	0.418
Sm	0.166		0.012		0.117	0.397	0.113	0.0186	0.0136	0.104			0.0726
Eu	0.0338	0.0029			0.0105	0.0372	0.007		0.0027	0.0102	0.0027		0.0052
Gd	0.1		0.0137		0.082	0.365	0.0731	0.0177		0.103			0.0606
Tb	0.0139	0.00149	0.00107		0.0097	0.0538	0.0088	0.00142		0.0161	0.00162		
Dy	0.072	0.0102	0.0095		0.0568	0.366	0.0494	0.0109		0.0976	0.0153	0.0058	0.0556
Ho	0.0142	0.00383	0.00189		0.0151	0.076	0.0114			0.0242	0.00457	0.00231	0.0164
Er	0.045	0.0094	0.0057		0.063	0.254	0.0383	0.0046		0.0656	0.0171	0.0072	0.0439
Tm	0.0046	0.00205	0.0022		0.0111	0.033	0.0084			0.0115	0.00402	0.00181	0.0091
Yb	0.043	0.0123	0.0168	0.0081	0.086	0.243	0.0623			0.0689	0.0293	0.0147	0.0931
Lu	0.0041	0.00397	0.00173	0.00193	0.0116	0.036	0.0084			0.014	0.007	0.00388	0.0205
Pb	2.03	0.253	0.041	0.088	0.0429	1.4	0.089	0.163	0.0408	0.0639	0.0175	0.0087	0.043
EREE	3.9586	0.17704	0.74029	0.30653	5.1068	11.912	4.3431	0.67432	0.8138	4.1331	0.43981	0.1742	2.3721

	MCT8_2	MCT8_6	S01_1	S01_2	S01_3	S01_4	S01_5	S01_6	S01_8	SN21_7	MCL9_1	MCL9_2	MCL9_3
	S(H). Mag.	S(H). Mag.	S(H). Mag.	S(H). Mag.	S(H). Mag.	S(H). Mag.	S(H). Mag.	S(H). Mag.	S(H). Mag.	S(H). Mag.	F. Mag.	F. Mag.	F. Mag.
Mg	1302	1583	1272	645	1063	1469	1128	1402	880	160	78	75.7	67.1
Al	1345	1791	137	63.6	94	143.7	86.7	151.1	248	345	138.7	115.3	91.1
P			167	5.7	107	25.4		20.7	35.9				
Ca	118		6990	80	193	183		153	320	1890	45		
Ti	1718	1971	664	706	789	755	743	775	634	4860	3848	3985	3900
V	2464	2484	1524	1523	1515	1516	1528	1502	1544	3486	2323	2311	2327
Cr													
Co	60.19	78.58	17.59	16.2	17.02	23.73	22.22	24.57	16.24	30.58	48.76	48.88	49.29
Ni	416.6	422.4	322.7	310.2	309.4	318.8	319.4	319.2	308.1	241.4	196.2	192.1	194.9
Y	0.326	0.0075	8.18	0.57	3.38	1.601	0.377	1.536	5.03	21.2	0.0185	0.0156	0.0735
La	0.374	0.0669	8.92	0.464	2.69	1.277	0.3378	1.277	3.9	0.227	0.015	0.0088	0.0158
Ce	1.25	0.0748	21.92	2.89	10.3	3.591	1.218	4.729	11.82	0.731	0.0443	0.0234	0.0428
Pr	0.139	0.0069	2.3	0.1781	0.788	0.42	0.1387	0.486	1.084	0.184	0.0045	0.00294	0.0046
Nd	0.47	0.0237	9	0.728	3.07	1.497	0.542	1.799	4.29	1.45	0.0163		0.0242
Sm	0.058		1.916	0.154	0.717	0.226	0.078	0.311	1.093	1.34			
Eu	0.0067		0.498	0.018	0.151	0.0245	0.0089	0.0286	0.308	0.473			
Gd	0.0582		1.984	0.125	0.74	0.191	0.072	0.212	1.25	2.31			
Tb	0.008		0.286	0.0177	0.117	0.0319	0.0105	0.0272	0.192	0.534	0.002		0.00218
Dy	0.0482		1.634	0.1044	0.689	0.238	0.0595	0.222	1.219	3.82			0.0086
Ho	0.0102		0.304	0.0193	0.1297	0.0653	0.0153	0.0608	0.225	0.84			0.0047
Er			0.827	0.0612	0.394	0.225	0.0404	0.219	0.619	2.68			0.0103
Tm	0.00327		0.1057	0.0087	0.055	0.036	0.0066	0.0303	0.0799	0.392	0.00086	0.0011	0.00205
Yb	0.0214		0.597	0.0533	0.31	0.236	0.0381	0.195	0.455	2.48		0.007	0.0224
Lu	0.00293		0.0787	0.0065	0.042	0.0331		0.0299	0.0607	0.378	0.00261	0.0015	0.0048
Pb	0.104	0.048	0.42	0.147	0.328		0.035	0.0298	0.925	0.564	0.0199	0.019	0.0546
EREE	2.4499	0.1723	50.3704	4.8282	20.1927	8.0918	2.5658	9.6268	26.5956	17.839	0.08557	0.04474	0.14243

magnetite-apatite mineralization and is characterized by white color albite (Mirzababaei, 2018) and the second phase is associated with pinkish colour albite, as well the first phase is much larger than the second phase in volume.

The calcic alteration is distinguished by actinolite replacing earlier minerals (Fig. 6B) and it occurs as a proximal feature and dominates all other alteration products with proximity to the ore zone (Heidarian et al., 2017). An argillic alteration can be distinguished overprinting other alteration types at surface and shallow depths (Fig. 4C).

Potassic alteration, overprinting earlier sodic and calcic alteration assemblages is represented by K-feldspar mantling albite grains and disseminated K-feldspar grains (Heidarian et al., 2017). $^{40}Ar/^{39}Ar$ dating of K-feldspar in altered rhyolitic rocks of Esfordi and Chadormalu deposits show ages of 131–303 and 159 Ma., respectively (Torab, 2008).

Sericitic alteration occurs as replacing original magmatic minerals associated with chlorite formation (Fig. 6C; Heidarian et al., 2017). Silicic alteration occurs as newly formed fine-grained quartz and overgrowths on the primary quartz (Heidarian et al., 2017). Calcite veinlets occur in altered host rocks and locally in the iron deposits (Fig. 6D).

3. Analytical methods

3.1. Mineral chemistry

Trace element analyses in magnetite made using LA-ICP-MS at Lund University, using a Teledyne Photon Machines G2 laser coupled to a Bruker Aurora Elite quadrupole ICP-MS. Calibration using NIST612, was aimed at obtaining high and stable signal counts and on low oxide production ($^{238}U/^{238}U^{16}O$ < 0.5%) and Th/U ratios around 1. Laser power was measured directly in the sample cell via an energy meter. Analytical sessions were setup to run automatically with standard-sample-standard bracketing, using BCR-2G (USGS) as primary standard and NIST610 as secondary standard. Fe57 was used as internal standard (assuming the following Fe concentrations: BCR-2G 9.6 wt%, NIST610

458 ppm and magnetite 72.4 wt%). Analyses were done with 210 shots at 7 Hz and a fluence of ca. 3–4 J/cm^2. In session S1, S5 and S07 a spot size of $55 \times 55\,\mu m$ and in session S6 a spot size of $30 \times 30\,\mu m$ was used. Baseline compositions were measured for 20 s before each spot analyses and subtraction was done with a step-forward approach. Data reduction was done following method described by Paton et al. (2011).

3.2. Oxygen isotopes

The magnetites were concentrated by jaw crushing, and washing in distilled water. Single magnetite grains were separated under a binocular microscope. Oxygen isotope data were obtained at the University of Cape Town. Approximately 20 mg of magnetite powder was reacted with ClF_3 for 6 h, and oxygen was extracted using a conventional silicate line at the University of Cape Town following the methods described in Harris and Ashwal (2002). The liberated O_2 was converted to CO_2 using a hot platinized carbon rod, and the isotope ratios were measured off-line using a Finnigan Delta XP mass spectrometer in dual-inlet mode. Data are reported (Table 2) in δ notation, where $\delta^{18}O = (R_{sample}/R_{standard} - 1) * 1000$, and R = the measured $^{18}O/^{16}O$ ratio. Duplicate 10 mg splits of an internal quartz standard (MQ) were run with each batch of 8 samples, and were used to convert the raw data to the SMOW scale using the $\delta^{18}O$ value of 10.1‰ for MQ obtained by calibration relative to NBS28. The long-term variability of MQ suggests a 2δ error of 0.16‰. Yields were measured using a pressure transducer connected to a small-volume cold finger. The quartz standard MQ gave average yields of 99.3 ± 1.7% (1ó, n = 3) whereas the magnetites gave yields which range from 92.2 to 111.2% (average 102.0 ± 5.9%, 1ó). The yields are important because they indicate that complete reaction was largely accomplished and that the contribution of oxygen from impurities with higher oxygen content (e.g. quartz) was minimal.

4. Results

4.1. Mineral chemistry

The chemical compositions of magnetite grains are presented in Table 1. Fig. 7A shows two analysed spots of massive magnetite by LA-ICP-MS. All analysed La-ICP-Ms data from different type of magnetites in various deposits show typical variation in different elements. The texture of the massive magnetite grains is not pristine and they have porous (Fig. 7). Smaller grains of magnetite can be observed within some magnetite grains (Fig. 7B). The SEM backscattered electron images (SEM-BSE) of the Chadormalu samples testify growing of two types of magnetites in the massive part of the deposit (Heidarian et al.,

Table 2
Representative Oxygen isotope (‰) of massive and foam-like magnetites from the Bafq district. (*from Moore and Modabberi, 2003)

Deposit	Sample	$\delta^{18}O$
Choghart	Massive- MCT03	4.44
Choghart	Massive-MCT07	2.97
Choghart	Massive-MCT08	4.46
Choghart	Massive-MCT21	5.27
Chadormalou	Massive-MCL07	4.09
Chadormalou	Massive-MCL19	4.22
Chadormalou	Foam-like MCL05	−0.45
Chadormalou	Massive-MCL13	2.87
Se Chahun XI	Massive-SN2	3.84
Se Chahun XI	Foam-like SN4	0.44
Se Chahun X	Massive-SN20	3.18
Se Chahun X	Massive-SN21	4.12
Choghart	Massive-Ch1*	3.66
Choghart	Massive-Ch2*	3.73
Choghart	Ch3*	4.12
Choghart	Ch4*	4.38
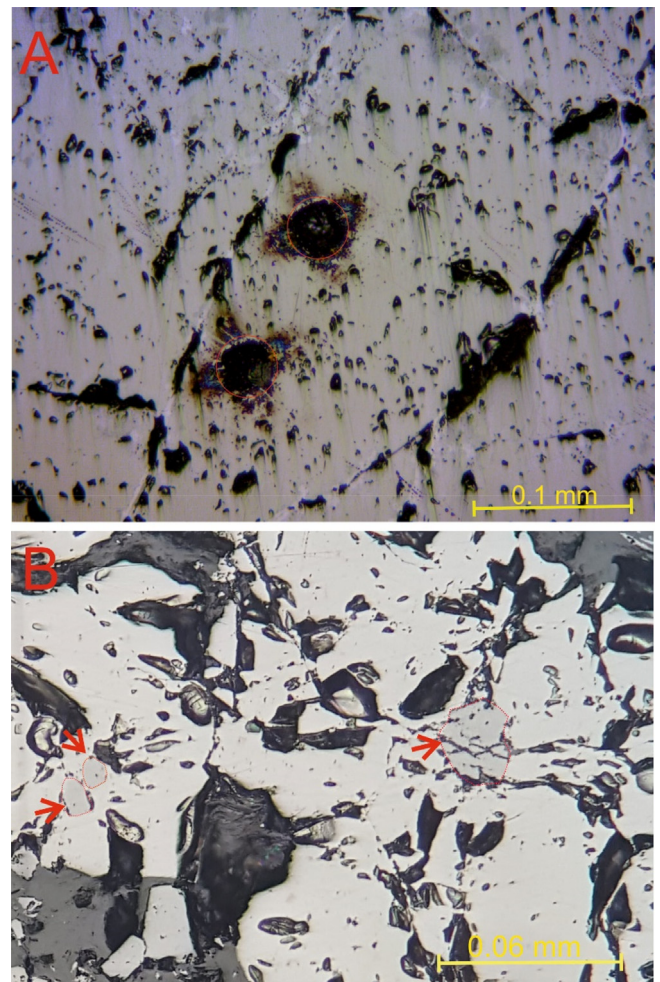
Fig. 7. Microscopic photo of a magnetite and two spots of analysis by LA-ICP-MS. Microscopic photo of the massive part showing primary igneous magnetite (mark by red colour), surrounded by the hydrothermal magnetite. (For interpretation of the references to color in this figure legend, the reader is referred to the web version of this article.)

2016). They don't show any zonation. Fractures of the massive part of ore and veins are filled with foam-like magnetite, showing mostly triple junctions zonation in back scattered electron (BSE) images is observed especially in some of these magnetites (Heidarian et al., 2016).

The analysed magnetites from the massive part (primary igneous) and late stage magnetites (high T-hydrothermal) form different deposits and locations in the Bafq district are comparable, however, data from the foam-like magnetite are limited. Three types of magnetites do not show clear diversity in the analysed elements, the only exception is REE contents of the foam-like magnetite. The variations of different elements vs. Mg content in magnetite grains are shown in Fig. 8. It seems that the most primary igneous magnetites have higher contents of Co, V, Ti, Al and Pb than surrounding hydrothermal magnetites in the massive part.

REE concentration in some magnetites is below the detection limits of LA-ICP-MS. Total REE (ΣREE) contents of magnetite from the primary (igneous) magnetite range from 0.04 to 50 ppm (average 8.4 ppm); ΣREE of magnetite from the surrounding parts (high T-hydrothermal) range from 0.17 to 50 ppm (average 9.3 ppm), and in foam-like magnetite range from 0.04 to 0.14 ppm. The most analysed magnetites display negative Eu-anomalies, relatively flat and HREE and LREE enrichment patterns (Fig. 9). Some analysed magnetites show positive slope from Dy to Lu, whereas some others show flat pattern in the HREE contents (Fig. 9). Negative Eu-anomalies are seen in some
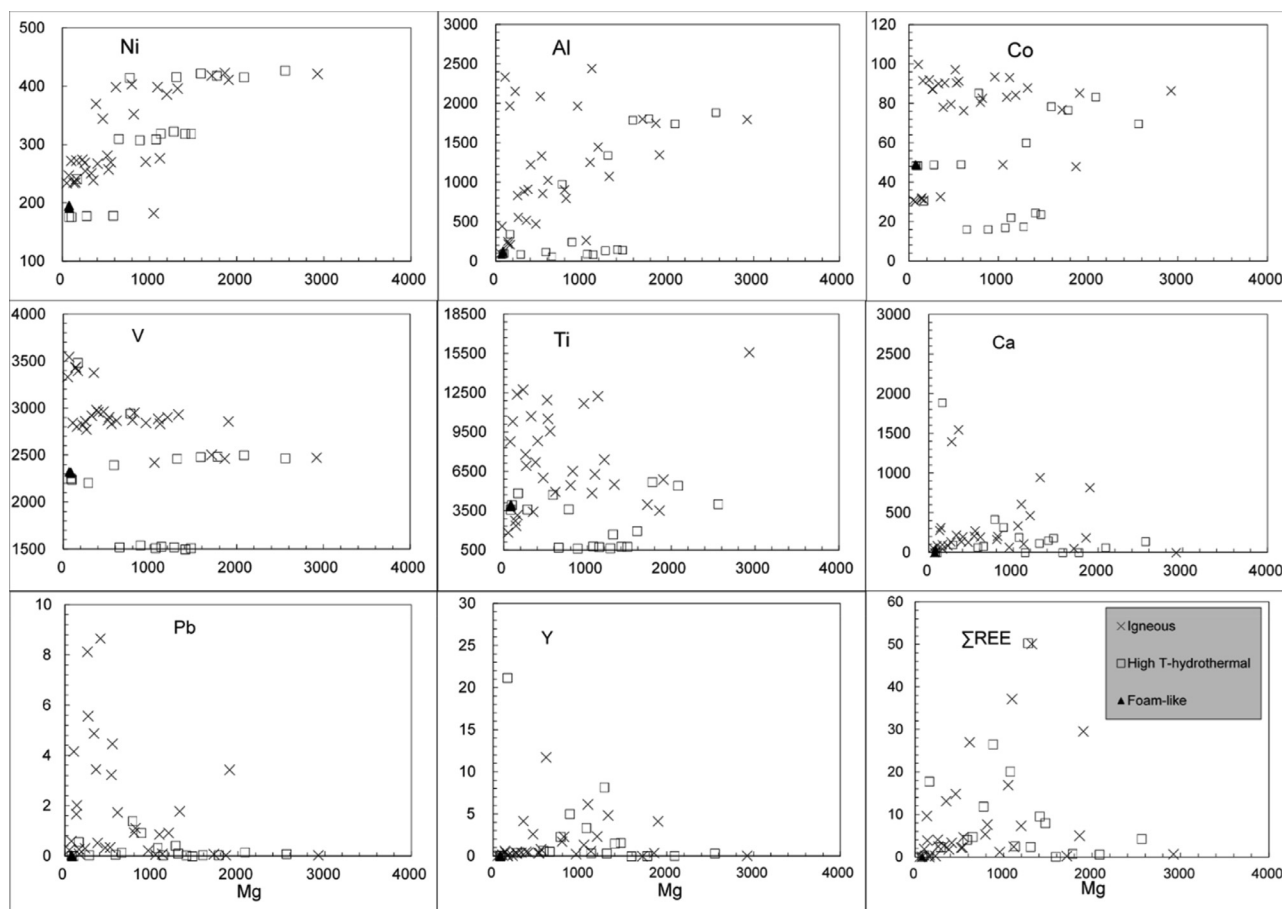
Fig. 8. The variation of trace elements relative to Mg in magnetites of Chadormalou, Se Chahun and Choghart deposits (elements in ppm).

samples. Eu/Eu* [Eu/Eu* = $(Eu_N/(SQR(Sm_N{}^*Gd_N))$]in primary (igneous) magnetite is 0.32–0.90 (La/Yb: 0.42–38.5) and in the surrounding part (high T-hydrothermal) is 0.24–0.82 (La/Yb: 0.06–11.7). We do not have Eu data for the Se Chahun foam-like magnetite but La/Yb is < 1 for this type of magnetite.

4.2. Oxygen isotopes

The $\delta^{18}O$ values of massive magnetites (Table 2) range from 2.87‰ to 5.27‰, which are markedly higher for the already analysed Choghart deposit (5.27‰). Our data are in good agreement with published data for the Choghart deposit by Moore and Modabberi (2003). The amounts of average, median and standard deviation for the analysed magnetites in this research and those from Moore and Modabberi (2003) are shown in Table 2. The foam-like magnetites have low $\delta^{18}O$ value of 0.44‰ and −0.45‰. The lowest $\delta^{18}O$ value obtained from the Chadormalou foam-like magnetites.

5. Discussion

5.1. Magnetite origin

According to some previous studies and this study, the Bafq magnetite-apatite deposits have distinct Kiruna-type characteristics. The V and Ti contents of the magnetite from the Se Chahun deposit are similar to El Laco deposits (in the Chilean Andes with Cainozoic age and magmatic to superheated hydrothermal origin; Velasco et al., 2016; Tornos et al., 2016) rather than Kiruna (Fig. 10).

Kiruna-type iron oxide-apatite (IOA) deposits are sometimes classified as the Cu-poor end-member of hydrothermal iron oxide copper-

gold (IOCG) deposits (e.g. Hitzman et al., 1992; Hitzman, 2000). Some authors have distinguished Kiruna-type IOA deposits from IOCG deposits in general (e.g. Williams et al., 2005; Knipping et al., 2015). Others assume degassing of an iron oxide magma at depth as source for IOCG forming fluids (Naslund et al., 2002). IOCG deposits are mostly thought to be formed by hydrothermal processes (e.g. Mumin et al., 2007; Barton, 2014), the origin of Kiruna type IOA deposits remains controversial. This type of deposits has been interpreted to have the hydrothermal-sedimentary (volcano-sedimentary) origin, the magmatic-hydrothermal transition origin, and the crystallization of P-rich iron oxides melts (magmatic) origin (e.g., Bookstrom, 1977; Hildebrand, 1986; Förster and Jafarzadeh, 1994; Nyström and Henríquez, 1994; Naslund et al., 2000, 2002; Sillitoe and Burrows, 2002, Tornos et al., 2011, 2016; Jami et al., 2007).

The compositional range of magnetite from Kiruna-type deposits in Ti + V (wt%) vs. Al + Mn (wt%) discrimination diagram form Dupuis and Beaudoin (2011) seem to overlap mostly with high-T hydrothermal magnetite, formed in environments such as porphyry, IOCG and Fe-Ti-V/P deposits and cannot be distinguished on any existing discrimination diagram (Knipping et al., 2015). Nadoll et al. (2014) proposed that Ti and V concentrations in magnetite could be used to discriminate igneous versus magmatic-hydrothermal magnetite. According to the data presented here, some studied magnetites plot in the igneous field and a few samples have affinity to the overlapping igneous and hydrothermal field (Fig. 11), which is consistent with generation by magmatic processes, specifically liquid immiscibility. However, the use of this discriminatory diagram for genesis interpretation is argued by Velasco et al. (2016) and Broughm et al. (2017) shortly after introducing. This is because Ti is incompatible element in oxidized melts (Frost and Lindsley, 1991). Foam-like magnetite of the Bafq district plot in the
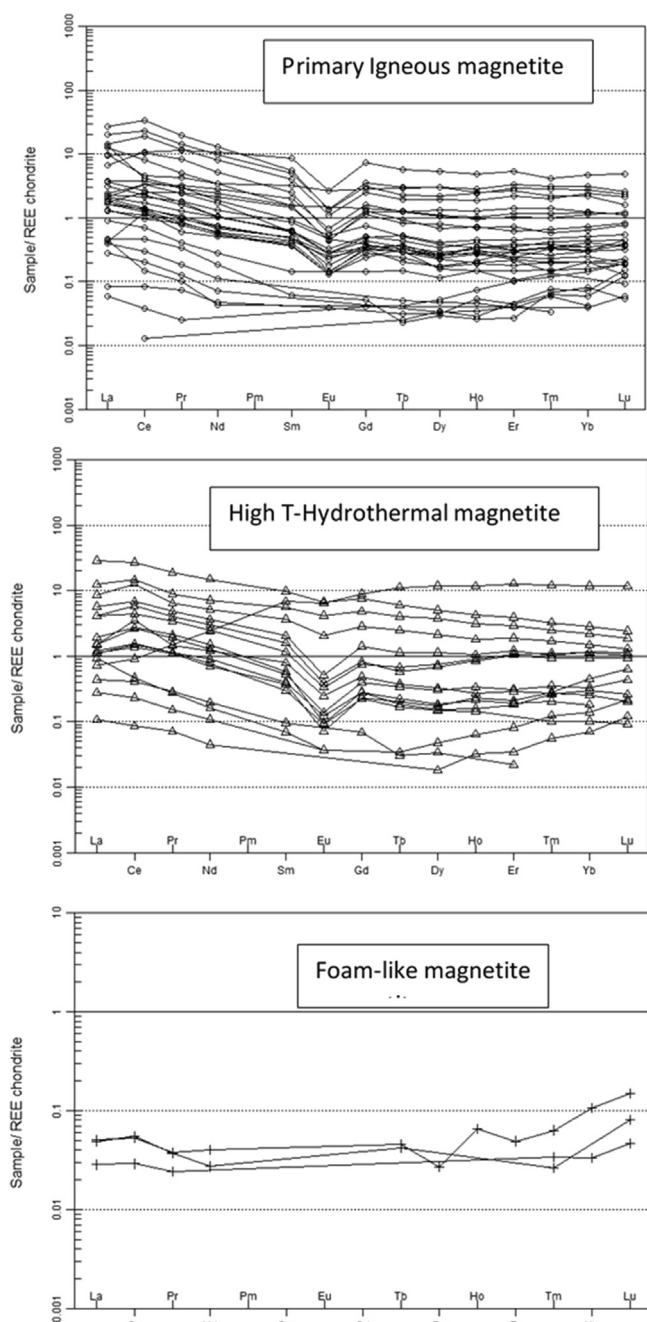
Fig. 9. Chondrite-normalized rare earth element patterns for magnetite from Chadormalou, Se Chahun and Choghart deposits. Normalization values are from Sun and McDonough (1989).
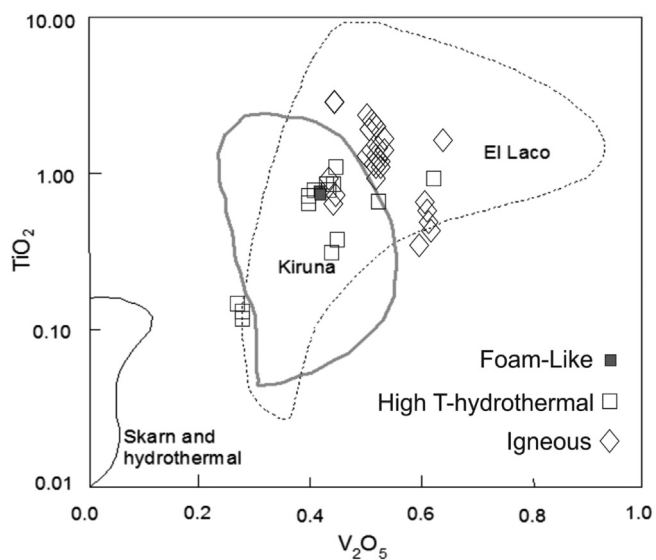

Fig. 10. Plot of V_2O_5 vs. TiO_2 content (wt.%) in magnetite by different genesis. Compositional fields for El Laco and Kiruna are from Nyström and Henríquez (1994); other data are from Ren (1991).
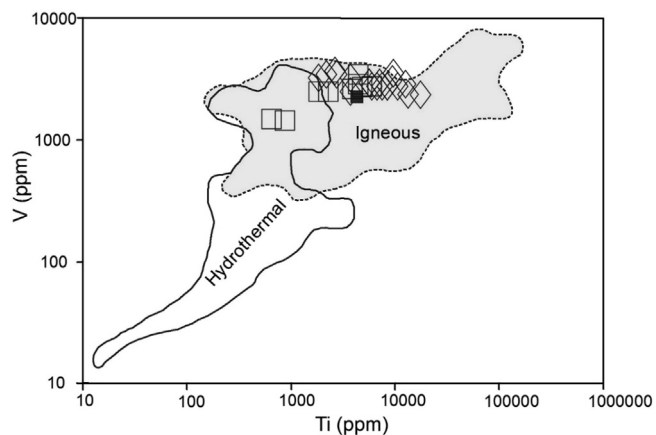

Fig. 11. Concentration of Ti vs. V in the studied magnetites. Diagram is from Knipping et al. (2015). Symbols as in Fig. 10.
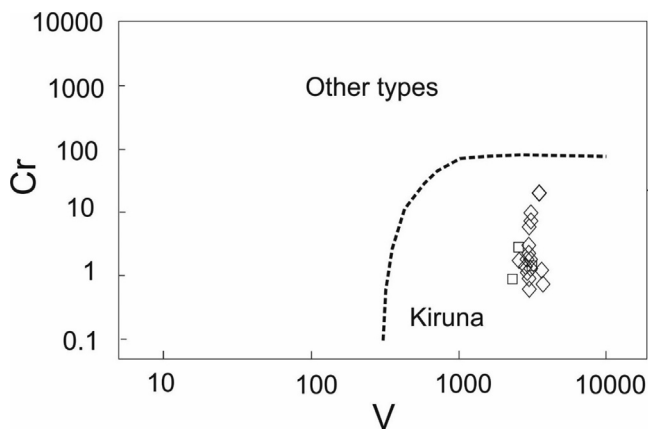
Fig. 12. Concentration of V (ppm) vs. Cr (ppm) in the studied magnetites. Diagram is from Knipping et al. (2015). Symbols are as in Fig. 10.

igneous field in this diagram and hydrothermal magnetite samples are scattered in the diagram. This diagram cannot reveal the origin of the Bafq magnetites, unequivocally.

Based on Cr depletion and V enrichment of magnetite from Kiruna-type deposits in Chile (El Romeral and El Laco), and in ore magnetite from Kiruna, Sweden (Nyström and Henríquez, 1994; Dare et al., 2015), and comparing the Cr and V content in other type of deposit (especially IOCG) Knipping et al. (2015) proposed a new discrimination diagram, they assign magnetite with Cr contents lower than ~100 ppm and V contents higher than ~500 ppm to Kiruna-type deposits. The studied deposits plot with the Kiruna-type deposits and away from the field for IOCG in the diagram of V vs. Cr in magnetite (Cr content in some studied magnetite samples was below detection limit of La-ICP-Ms; Fig. 12). New magnetite analyses from the Kiruna and El Laco

magnetite-apatite ores by Broughm et al. (2017) indicate that the defined fields in the diagram is not perfectly correct. Because, some data of theses magnetites plot in the IOCG and porphyry deposits fields.

The $d^{18}O$ values from the studied deposits from Iran are plotted on
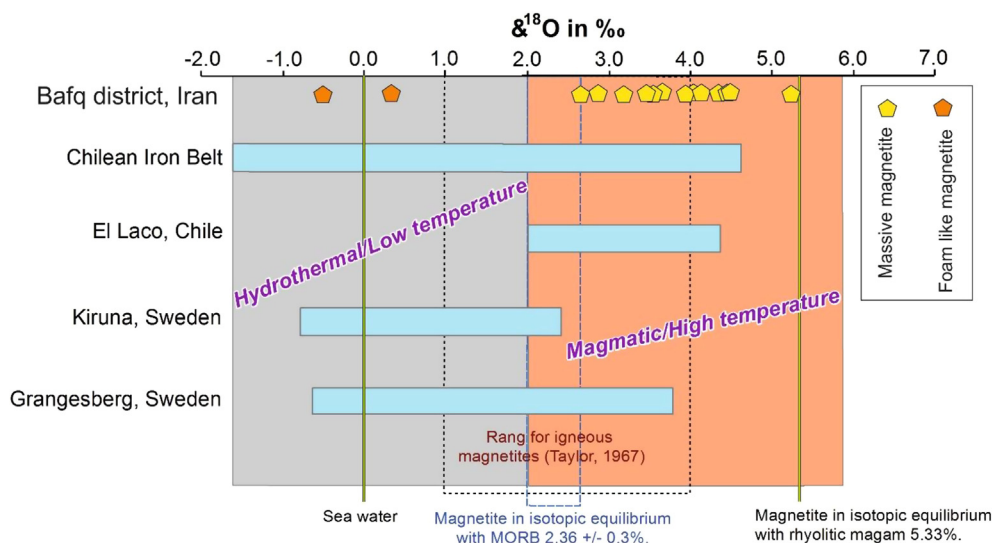
Fig. 13. $\delta^{18}O$ values of magnetites from the studied deposits compared to other volcanic-hosted iron ore deposits. The diagram is from Nyström et al. (2008), Grangesberg data from Johnsson et al. (2013).

the diagram of Nyström et al. (2008) that shows oxygen isotope values for magnetite from some deposits (Fig. 13). A distinct similarity can be observed between the values of the studied magnetites with the Chilean Iron Belt deposits. However, magnetite samples from the Bafq district mostly plot in the range of the El Laco deposit. Most of the studied samples plot in the magmatic or high-temperature hydrothermal field in this diagram. Only foam-like magnetites plot in the hydrothermal field.

Dare et al. (2015) believe that the low Ti content in the Kiruna-type magnetite is indicative of a hydrothermal origin. According to this, magnetites of the Se Chahun X deposit have lowest Ti content, comparing to other deposits, so the generation could be related to hydrothermal process. However, Velasco et al. (2016) clearly show that not all magmatic magnetites are Ti-rich. Concentration of Al, Cr, Ni, V, Y, Co, Ti and REE, which are incompatible during partial melting but not as readily mobile in hydrothermal fluids, are variable in the studied magnetites and some elements (Ti, Cr, REE, Al, Co) in different studied magnetites are scattered in Fig. 8. This significant variation in the compatible elements in the Bafq magnetites could be related to the re-equilibration between the magnetite and the partial melts that may occur during the onset or during the oxy-exsolution at shallow depths prior to magma eruption, similar to process proposed for El Laco deposit by Velasco et al. (2016).

The Cr content in the studied magnetites is low or below detection limit. Kiruna-type magnetite has low Cr content, explained by the high mobility of Cr^{6+} into oxidized fluids that transported Cr out of the system, or its high KD into augite prior to crystallization of magnetite (Broughm et al., 2017). The lack of relation of augite crystallization to magnetite formation and presence of hydrous magmatism (oxidized arc-magma) in the Bafq district could indicated domination of oxidized condition for iron deposit formation in Bafq. The iron-rich melt became more oxidized as it moved closer to the surface (Broughm et al., 2017). Ti in the oxidized melts is an incompatible element (Frost and Lindsley, 1991). In an oxidized system, the rate of Fe^{3+} increases, which primarily occupies the octahedral sites in magnetite, so the incorporation of other elements (such as Ti) in the iron-rich melt is prohibited. The TiO_2/FeO ratios in the massive magnetite (max: 0.13, average: 0.003) are higher than ratios in the foam-like magnetite (max: 0.0051, average: 0.00076) in the Chadormalou deposit (Heidarian et al., 2016). The Ti/Fe ratio in the magnetite from the massive parts of the studied deposits shows Ti depletion trend in the immiscible iron melt, based on data by Torab (2008) (min: 0.16, max: 4.9, average: 0.7). It could indicate that the melt lost most of Ti during immiscibility, and probably

fractionate into the parental silicate melt (e.g. Velasco et al., 2016). The Ti/Fe ratio in magnetite indicates coupled substitution to maintain charge balance in different condition of mineralization environment (e.g. Waychunas, 1991). Octahedral sites in the magnetite structure are randomly occupied by subequal numbers of ferric (Fe^{3+}) and ferrous (Fe^{2+}) iron atoms, whereas the tetrahedral sites are exclusively occupied by the smaller ferric iron atoms $Fe^{3+}[Fe^{2+} Fe^{3+}]O_4$ (Lindsley, 1976; Waychunas, 1991). Above 600 °C a continuous solid solution exists between magnetite and ulvöspinel (titanomagnetite) and its oxidation products (titanomaghemite) with coupled substitution of Ti^{4+} for Fe^{3+} in the octahedral sites and Fe^{2+} for Fe^{3+} in the tetrahedral sites (Waychunas, 1991; White et al., 1994). Poorly constrained and extensive miscibility gaps occur below 600 °C (Ghiorso and Sack, 1991). In addition to chemical composition of some magnetites that show affinity to magmatic source, the physical features of the magnetite bodies in the Bafq district (such as presence of miarolitic cavities or tubes, lava flows texture of ore, and lack of systematic relation of mineralization to the hydrothermal alteration zones) also, support a magmatic origin for the deposits. Tornos et al. (2016) believe that tubes (miarolitic cavities) in the magnetite ores never could form by hydrothermal replacement process. However, the presence of signatures of brecciation in local scale (in some ore bodies such as Se Chahun) could be indicative of hydrothermal origin. However, if the whole ores formed through hydrothermal process, the unrealistic volume of fluid was needed to form the Bafq deposits (1,800,000 bt of high grad Fe ore, NISCO, 1980). If we assume an external source (meteoric waters) for extensive hydrothermal fluid, a long lasting shallow depth high-temperature heat source is needed for precipitation of all the magnetite in a rather isothermal hydrothermal system. This heat source is not documented in the Bafq district. Therefore, a combined igneous and magmatic-hydrothermal source is more reasonable for magnetites of massive parts and a low temperature hydrothermal source for the foam-like magnetite in veins and micro fractures.

5.2. Genesis mechanism

Generally, magnetite can host low to zero contents of REE and Ca in its lattice (e.g. Wood et al., 1991). Some massive part magnetites of the Bafq district have relatively considerable amounts of REE and Ca. Probably the measured relatively high REE and Ca are from invisible nano-inclusions (such as apatite).

The correlation of REE patterns of magnetite (presumably in nano-inclusions) with magmatic rocks could indicate immiscible iron-rich

melt formation in the parental magma. REE patterns in the studied magnetites are the same as REE patterns in unaltered Bafq district magmatic rocks (Ramezani and Tucker, 2003; Torab, 2008; Gol Karam et al., 2011; Khoshnoodi et al., 2017) and apatite (Bonyadi et al., 2011; Heidarian et al., 2018). They display remarkably negative Eu anomalies and enrichment in LREE. It probably indicates same origin for ore deposit and magmatic rocks. It seems that apatite controls the REE budget of this magmatic system. So, the apatites in the ore have higher ΣREE concentrations and more significantly negative Eu anomalies than magmatic rocks and magnetite.

Three mechanisms are proposed for formation of magmatic magnetite and immiscibility of the Fe-rich melt from a silicate magma: (1) crystal fractionation, (2) magma mixing; or (3) crustal contamination (Wilson, 1989; Zhou et al., 2005). The magmatic rocks of the Bafq district are calc-alkaline without evidence for magma mixing. Therefore, the role of fractional crystallization (correlated with tholeiitic magma, Velasco et al., 2016) and magma mixing mechanisms for immiscibility of Fe-rich melt in Bafq distinct is unlikely. The crustal contamination is the most plausible process for iron-rich melt immiscibility.

The crustal contamination could be occurred either via assimilation of host rocks or by mingling with crustal-derived melts. The experimental works show that the additions of even minor amounts of phosphorous appear to have significant effects on liquid immiscibility, even in anhydrous systems (e.g. Lledó, 2005; Hou et al., 2010). Phosphorous dramatically reduces the viscosity of silicate melts (London et al., 1993). Old studies postulated that high sodium contents in the silicate magmas also play an important role in forming immiscible liquids (Philpotts, 1967). Moreover, adding P or Na to silicate magma, variation of Cl, F, H_2O contents and/or changes in fO_2 during magma crystallization produce immiscible liquids, rich in Fe, Mg, Ca, Ti, P and O (Naslund, 1983; Veksler et al., 2007). Due to presence of phosphorous agent (apatite) in the studied deposits, more likely addition of P to the primary magma has important role in immiscible Fe-rich melt formation. In addition, the secondary variscite $(AlPO_4(H_2O)_2)$ veins along Pb-Zn ores in the Koushk deposit (a SEDEX-type deposit; Rajabi et al., 2012) may have been caused by P recycling in the district during Cambrian. The Early Cambrian formation is the most likely unit for source of contamination of primary magma. The Early Cambrian Soltanieh Formation (or its equivalent) is known for its phosphorite-bearing marine sedimentary rocks. Isotope and geochemistry data of Torab (2008) in the Esfordi deposit show that apatite generated from liquids derived from Soltanieh Formation. Hushmandzadeh (1989) found some units of this formation in the distinct areas of the Bafq district (below 150 m in thickness). The Early Cambrian unit in the Bafq district includes evaporitic rocks (e.g. Samani, 1993). The contamination of magma with P and evaporate derived from Early Cambrian units led to separation a Fe-rich melt at depth. Some primary igneous magnetite crystallized in this condition. Iron-rich melt (with crystalized primary magnetites) may not simply ascend or erupt. However, concentration of volatiles in the iron-rich melt caused separation and ascending of iron-rich melt from silicate melt due to contrasts in viscosity and density (e.g. Tornos et al., 2017). This fluid system rose to the surface, where the whole Fe-rich melt crystallized.

Exsolving magmatic-hydrothermal fluid prefers to nucleate bubbles initially on crystallized magnetite surface with decreasing surface energy, due to larger wetting angles of fluid and oxides (magnetite) than other crystallized silicate minerals such as presented model for generation of the Chilean Iron Belt by Knipping et al. (2015). The magmatic-bubble pairs ascent through the magma chamber and sweep up other magnetite microlites. Since H_2O saturation is followed by significant partitioning of halogens (Cl, F) into the fluid phase, the exsolving fluid will became halogens-rich, which in turn has the ability to scavenge from silicate melt up to several wt% Fe as Fe-halogen complex (Knipping et al., 2015). According to REE patterns of studied magnetites and Taylor and Feyer (1983) suggestion, the main halogen agent in

the fluid phase of Bafq was Cl-rich fluid. They suggest that LREEs are preferentially mobilized in Cl-rich fluids, whereas F and CO_2-bearing fluids are rich in HREE. It is possible the chlorides and volatiles were derived from the dissolution of ancient evaporites during contamination. Originally igneous magnetite continues to grow by surrounding Fe complex in the fluid and characteristics of these new growing magnetites tend to high temperature hydrothermal magnetite. The partition of igneous and hydrothermal magnetites are different in the various locations of the Bafq deposits, so that a part of a deposits may formed from just one type of magnetite.

The crystallization of titanite or rutile after crystallization of initial igneous magnetites, during hydrothermal process and occasional U-Th-REE enrichment indicate the first stage of Na-Ca alteration effects on the iron ores. The iron generation and sodic alteration are close in age (Bonyadi et al., 2011). According to proposed genetic model for El Laco deposit by Tornos et al. (2017), the ascent and crystallization of iron-rich melt to the shallow depth resulted in separation of an aqueous fluid in the form of dominant vapor and small amounts of hypersaline brine. This event promotes the exsolution of superheated hydrothermal fluids. This high-temperature brine includes the incompatible elements such as Na, K, Ti, (± U, Th, REE) and excess Ca, Mg and Fe reacted with the host rocks. The predominant ascending low-density vapor phases would have formed argillitic alteration zones in the host rocks. Nonetheless, the hydrothermal process doesn't preclude a role for immiscible Fe-oxide–P-rich melts in the initial stages of the mineralising process. Titanium cannot incorporate into magnetite during oxidizing at the initial magnetite mineralization and there is not enough Ca and Si for titanite formation (Velasco et al., 2016). So, they (or other elements such as U, Th, or REE) concentrate in the hypersaline brine as incompatible elements while the rate of Ca and Si were enough for formation of titanite (or thorite, uraninite, davidite, monazite). Titanite destabilized to rutile following alteration. The giving temperature of > 700 °C for sodic-calcic metasomatism by two actinolite-magnetite isotope pairs in the Saghand (anomaly 5) area (iron bodies have not outcrop at surface and mineralization occur in depth) could indicates the minimum temperature of hydrothermal fluid of mineralization in the Bafq district; Poshte-e-Badam block (Deymar et al., 2018).

Replacement of magnetite by hematite (± goethite) or the foam-like magnetite in the Bafq deposits and filling fractures of thorite by iron-oxides (magnetite) are signature of the alteration, post-crystallization and indicate that degassing continued at depth, likely related to the crystallization of iron-rich melts in a gradually cooling system (Tornos et al., 2016), which recrystallized the massive magnetite and then the foam-like magnetite.

6. Conclusions

We report in–situ LA–ICP–MS trace element analyses of magnetite and O-isotopes values from the massive parts of three large (Choghart, Se Chahun and Chadormalou) magnetite-apatite deposits in the Bafq district in Central Iran. Based on the data and observations presented above, we draw the following conclusions.

- There are three types of magnetite. The massive parts include igneous and high-temperature hydrothermal magnetites and foam-like magnetite is in the veins and microfractures of massive part. The lack of zonation, higher Ti/Fe ratios and $\delta^{18}O$ values of > 2‰ indicates that massive magnetite formed at high temperature. The foam-like magnetites show zonation, lower ratios of Ti/Fe and $\delta^{18}O$ values of < 2‰ indicative of low temperature formation.
- The deposits (the massive parts) are Kiruna-type IOA with a magmatic (liquid immiscibility) to high-temperature hydrothermal origin, mostly similar to El Laco iron deposit.
- The liquid immiscibility was triggered by addition of phosphorus and evaporates during crustal contamination of the parental magma.
- The emplacement and crystallization of iron-rich melt in the shallow

depth promoted the exsolution of superheated hydrothermal fluids forming hypersaline fluid. This fluid led to sodic-calcic alteration and Th-U-REE mineralization related to high-temperature magnetite-apatite mineralization. The halogens-rich exsolving fluid has the ability to scavenge Fe from a silicate melt by several Fe-halogen complexes. This process let to the magmatic magnetite growth or nucleation of new magnetites from the iron-rich magmatic-hydrothermal fluid.

- Degassing process at depth was a long-standing event in the Bafq district, because it influenced primary magnetite and titanites, and cause recrystalized some magnetite and formed foam-like magnetite.

Acknowledgments

References

Aftabi, A., Mohseni, S., Babeki, A., Azaraein, H., 2009. Fluid inclusion and stable isotope study of the Esfordi apatite–magnetite deposit, Central Iran-a discussion. Econ. Geol. 104, 137–140. https://doi.org/10.2113/gsecongeo.104.1.137.

Aghanabati, A., 2006. In: Geology of Iran. Geological Survey of Iran, Tehran, pp. 586 [In Persian].

Barton, M.D., 2014. Iron oxide (–Cu–Au–REE–P–Ag–U–Co) systems. In: Holland, H., Turekian, K. (Eds.), Treatise of Geochemistry, pp. 515–536.

Bonyadi, Z., Davidson, G.J., Mehrabi, B., Meffre, S., Ghazban, F., 2011. Significance of apatite REE depletion and monazite inclusions in the brecciated Se-Chahun iron oxide-apatite deposit, Bafq district, Iran: insights from paragenesis and geochemistry. Chem. Geol. 281, 253–269. https://doi.org/10.1016/j.chemgeo.2010.12.013.

Bookstrom, A.A., 1977. The magnetite deposits of El Romeral, Chile. Econ. Geol. 72, 1101–1130.

Broughm, S., Hanchar, J.M., Tornos, F., Attersley, S., Westhues, A., 2017. Mineral chemistry of magnetite from magnetite-apatite ores and their host rocks in Sweden and Chile. Miner. Deposita 52 (8), 1223–1244. https://doi.org/10.1007/s00126-017-0718-8.

Daliran, F., 1999. REE geochemistry of Bafq apatites, Iran; implication for the genesis of Kiruna-type iron ores. In: Stanley (Ed.), Mineralium Deposita, Processes to Processing. Balkema, Rotterdam, pp. 631–634.

Daliran, F., 2002. Kiruna-type iron oxide-apatite ores and apatitites of the Bafq district, Iran, with an emphasis on the REE geochemistry of their apatites. In: Porter, T.M. (Ed.), Hydrothermal Iron Oxide Copper-Gold and Related Deposits: A Global Perspective. PGC Publishing, Adelaide Australia, pp. 303–320.

Daliran, F., Stosch, H.-G., Williams, P.J., Jamali, H., Dorri, M.-B., 2010. Early Cambrian iron oxide-apatite-REE (U) deposits of the Bafq district, East-Central Iran. In: Louise, Corriveau, Hamid, Mumin (Eds.), Exploring for Iron Oxide Copper-Gold (Ag-Bi-Co-U) Deposits: Examples from Canada and Global Analogues, pp. 147–160.

Dare, S.A.S., Barnes, S.-J., Beaudoin, G., Méric, J., Boutroy, E., Potvin-Doucet, C., 2014. Trace elements in magnetite as petrogenetic indicators. Miner. Deposita 49, 785–796.

Dare, S.A.S., Barnes, S.-J., Beaudoin, G., 2015. Did the massive magnetite "lava flows" of El Laco (Chile) form by magmatic or hydrothermal processes? New constraints from magnetite composition by LA-ICP-MS. Miner. Deposita 50, 607–617.

Deymar, S., Yazdi, M., Rezvanianzadeh, M.R., Behzadi, M., 2018. Alkali metasomatism as a process for Ti–REE–Y–U–Th mineralization in the Saghand Anomaly 5, Central Iran: insights from geochemical, mineralogical, and stable isotope data. Ore Geol. Rev. 93, 308–336.

Dupuis, C., Beaudoin, G., 2011. Discriminant diagrams for iron oxide trace element fingerprinting of mineral deposit types. Miner. Deposita 46, 319–335.

Eslamizadeh, A., 2017. Petrology and geochemistry of early cambrian volcanic rocks hosting the Kiruna-type iron ore in anomaly 10 of Sechahun, Central Iran. Iran. J. Sci. 28 (1), 21–35.

Foose, M.P., McLelland, J.M., 1995. Proterozoic low-Ti iron oxide deposits in New York and New Jersey; relation to Fe oxide (Cu–U–Au-rare earth element) deposits and tectonic implications. Geology 23, 665–668.

Förster, H., Jafarzadeh, A., 1994. The Bafq mining district in Central Iran: a highly mineralized Infracambrian volcanic field. Econ. Geol. 89, 1697–1721.

Frietsch, R., Perdahl, L.-A., 1995. Rare earth elements in apatite and magnetite in Kiruna-type iron ores and some other iron ore types. Ore Geol. Rev. 9, 489–510.

Frost, B., Lindsley, D., 1991. Chapter 12. Occurrence of iron-titanium oxides in igneous rocks. In: Linsley, D.H. (Ed.), Oxide Minerals: Petrologic and magnetic significance Reviews in Mineralogy. Mineralogical Society of America, pp. 433–468.

Geijer, P., 1931. The iron ores of Kiruna-type. Geographical distribution, geological characters and origin. Sver. Geol. Unders. Ser. C. 367 39p.

Ghiorso, M.S., Sack, O., 1991. Fe-Ti oxide geothermometry: thermodynamic formulation and the estimation of intensive variables in silicic magmas. Contrib. Miner. Petrol. 108, 485–510.

Gol Karam, S., Rashidnagad Omran, N., Masoudi, F., Vahabzadeh, G., 2011. The Zarigan granite: magmatic or metasomatic? J. Sci. Tarbiat Moallem Univ. Iran 10 (2), 825–840 [In Persian].

Haghipour, A., Pelissier, G., 1977. Geology of the Saghand Sector. In: Haghipour, A., Valeh, N., Pelissier, G., Davoudzadeh, M. (Eds.), Explanatory Text of the Ardekan Quadrangle Map, GSI H8, pp. 10–68.

Harris, C., Ashwal, L.D., 2002. The origin of low ??^{18}O granites and related rocks from the Seychelles. Contrib. Miner. Petrol. 143, 366–376.

Heidarian, H., Lentz, D., Alirezaei, S., McFarlane, C., Peighambar, S., 2018. Multiple Stage Ore Formation in the Chadormalu Iron Deposit, Bafq Metallogenic Province, Central Iran: evidence from BSE Imaging and Apatite EPMA and LA-ICP-MS U-Pb Geochronology. Minerals 8, 87. https://doi.org/10.3390/min8030087.

Heidarian, H., Lentz, D., Alirezaei, S., Peighambari, S., Hall, D., 2016. Using the chemical analysis of magnetite to constrain various stages in the formation and genesis of the Kiruna type Chadormalu magnetite-apatite deposit, Bafq district, Central Iran. Mineral. Petrol. 110 (6), 927–942. https://doi.org/10.1007/s00710-016-0437-3.

Heidarian, H., Saeed Alirezaei, S., Lentz, D.R., 2017. Chadormalu Kiruna-type magnetite apatite deposit, Bafq district, Iran: insights into hydrothermal alteration and petrogenesis from geochemical, fluid inclusion, and sulfur isotope data. Ore Geol. Rev. 83, 43–62 doi.org/10.1016/j.oregeorev.2016.11.031.

Hildebrand, R.S., 1986. Kiruna-type deposits: their origin and relationship to intermediate subvolcanic plutons in the Great Bear Magmatic Zone, northwest Canada. Econ. Geol. 81, 640–659.

Hitzman, M.W., 2000. Iron oxide-Cu-Au deposits: what, where, when, and why. In: Porter, T.M. (Ed.), Hydrothermal Iron Oxide Copper-Gold and Related Deposits: A Global Perspective. PGC Publishing, Adelaide Australia, pp. 9–25.

Hitzman, M.W., Oreskes, N., Einaudi, M.T., 1992. Geological characteristics and tectonic setting of Proterozoic iron oxide, copper- uranium-gold-REE deposits. Precambr. Res. 58, 241–287.

Hou, T., Zhang, Z.C., Encarnacion, J., Du, Y.S., Zhao, Z.D., Liu, J.L., 2010. Geochemistry of Late Mesozoic dioritic porphyries associated with Kiruna-style and stratabound carbonate-hosted Zhonggu iron ores, Middle-Lower Yangtze Valley, Eastern China: constraints on petrogenesis and iron sources. Lithos 119, 330–344 doi.org/10.1016/j.lithos.2010.07.009.

Hushmandzadeh, A., 1989. An introduction to the geology of the Biabanak-Bafgh region. In: Proceeding of the seminar on reserves and mining potential of the Yazd department 1988. Ministry of Mines and Metals, pp. 341–371 [In Persian].

Jami, M., 2005. Geology, Geochemistry and Evolution of the Esfordi Phosphate – Iron Deposit, Bafq Area, Central Iran. Unpublished Ph.D. Thesis. University of New South Wales.

Jami, M., Dunlop, A.C., Cohen, D.R., 2007. Fluid inclusion and stable isotope study of Esfordi apatite-magnetite deposit, Central Iran. Econ. Geol. 102, 1111–1125. https://doi.org/10.2113/gsecongeo.102.6.111.

Johnsson, E., Troll, V.R., Hoegdahl, K., Harris, C., Weis, F., Nilsson, K.P., Skelton, A., 2013. Magmatic origin of giant 'Kiruna-type' apatite-iron oxide ores in Central Sweden. Nat. Sci. Rep. 3, 1644–1652.

Khoshnoodi, K., Behzadi, M., Gannadi-Maragheh, M., Yazdi, M., 2017. Alkali metasomatism and Th-REE-mineralization in the Choghart deposit, Bafq district, Central Iran. Geologia Croatica 70 (1), 53–69. https://doi.org/10.4154/gc.2017.03.

Knipping, J.L., Bilenker, L.D., Simon, A.C., Reich, M., Barra, F., Deditius, A.P., Wälle, M., Heinrich, C.A., Holtz, F., Munizaga, R., 2015. Trace elements in magnetite from massive iron oxide-apatite deposits indicate a combined formation by igneous and magmatic-hydrothermal processes. Geochim. Cosmochim. Acta 171, 15–38. https://doi.org/10.1016/j.gca.2015.08.010.

Lindsley, DH., 1976. The crystal chemistry and structure of oxide minerals as exemplified by the Fe-Ti oxides. In oxide minerals. Mineral. Soc. Am. Short Course Notes 3, L-1 to L-60.

Lledó, H., 2005. Ph.D. thesis In: Experimental Studies on the Origin of Iron Deposits, and Mineralization of Sierra La Bandera, Chile. State University of New York, Binghampton, pp. 282.

London, D., Morgan, G.B., Babb, H.A., Loomis, J.L., 1993. Behavior and effects of phosphorus in the system Na$_2$O-K$_2$O-Al$_2$O$_3$–SiO$_2$–P$_2$O$_5$–H$_2$O at 200 MPa (H$_2$O). Contrib. Miner. Petrol. 113, 450–465.

Mirzababaei, G.R., 2018. Mineralogy, Geochemistry and Mineralization of Trace and Rare Earth Elements in Se-Chahun Ore Deposit, Bafq, Yazd. Unpublished Ph.D. thesis (in Persian). Shahid Beheshti University, Tehran, Iran.

Mohseni, S., Aftabi, A., 2015. Structural, textural, geochemical and isotopic signatures of synglaciogenic Neoproterozoic banded iron formations (BIFs) at Bafq mining district (BMD), Central Iran: the possible Ediacaran missing link of BIFs in Tethyan metallogeny. Ore Geol. Rev. 71, 215–236. https://doi.org/10.1016/j.oregeorev.2015.05.018.

Mokhtari, M.A.A., 2013. Genesis of iron-apatite ores in Posht-e-Badam Block (Central Iran) using REE geochemistry. J. Earth Syst. Sci. 122, 795–807.

Moore, F., Modabberi, S., 2003. Origin of Choghart iron oxide deposit, Bafq District, Central Iran: new isotopic and geochemical evidence. J. Sci. Islamic Republic Iran 14 (3), 259–269.

Mumin, A.H., Corriveau, L., Somarin, A.K., Ootes, L., 2007. Iron oxide copper-gold-type polymetallic mineralization in the Contact Lake Belt, Great Bear Magmatic Zone,

Northwest Territories, Canada. Explor. Min. Geol. 16, 187–208. https://doi.org/10.2113/gsemg.16.3-4.187.

Nadoll, P., Angerer, T., Mauk, J.L., French, D., Walshe, J., 2014. The chemistry of hydrothermal magnetite: a review. Ore Geol. Rev. 61, 1–32. https://doi.org/10.1016/j.oregeorev.2013.12.013.

Naslund, H.R., 1983. The effect of oxygen fugacity on liquid immiscibility in iron-bearing silicate melts. Am. J. Sci. 283, 1034–1059.

Naslund, H.R., Aguirre, R., Dobbs, F.M., Henriquez, F.J., Nystrom, J.O., 2000. The Origin, emplacement, and eruption of ore magmas. IX Congreso Geologico Chileno Actas 2, 135–139.

Naslund, H.R., Henriquez, F., Nyström, J.O., Vivallo, W., Dobbs, F.M., 2002. Magmatic iron ores and associated mineralization: examples from the Chilean high Andes and coastal cordillera. In: Porter, T.M. (Ed.), Hydrothermal Iron Oxide Copper-gold and Related Deposits a Global Perspective. PGC Publishing, Adelaide, pp. 207–226.

NISCO, 1980, Result of search and valuation works at magnetic anomalies of the Bafq iron ore region during 1976–1979, un-publication report, National Iranian Steel Corporation, p. 260.

Nyström, J., Henríquez, F., 1994. Magmatic features of iron ores of the Kiruna type in Chile and Sweden: ore textures and magnetite geochemistry. Econ. Geol. 89, 820–839.

Nyström, J.O., Billström, K., Henríquez, F., Fallick, A.E., Naslund, H.R., 2008. Oxygen isotope composition of magnetite in iron ores of the Kiruna type in Chile and Sweden. GFF 130, 177–188.

Paton, C., Hellstrom, J., Paul, B., Woodhead, J., Hergt, J., 2011. Iolite: freeware for the visualisation and processing of mass spectrometric data. J. Anal. At. Spectrom. 26 (12), 2508–2518. https://doi.org/10.1039/c1ja10172b.

Philpotts, A.R., 1967. Origin of certain iron-titanium oxide and apatite rocks. Econ. Geol. 62, 303–315.

Rajabi, A., Rastad, E., Alfonso, P., Canet, C., 2012. Geology, ore facies, and sulphur isotopes of the Koushk vent-proximal sedimentary-exhalative deposit, Posht-e Badam Block, Central Iran. Int. Geol. Rev. 54 (14), 1635–1648. https://doi.org/10.1080/00206814.2012.659106.

Ramezani, J., Tucker, R.L., 2003. The Saghand region, Central Iran: U-Pb geochronology, petrogenesis and implications for Gondwana tectonics. J. Am. Sci. 303, 622–665. https://doi.org/10.2475/ajs.303.7.622.

Ren, Q.J., 1991. Studies of Ti–Fe Oxides in Igneous Rocks and Related Deposits. Science Press, Beijing [In Chinese].

Sadeghi Davati, V.A., Hassanzadeh, J., Alirezaei, S., 2008. Iron Oxide- apatite mineralization of Bafq district: spatial, temporal and geochemical relationship with granitoid magmatism and early Cambrian sedimentary provinces. 26th Earth Sciences Meting. Geological survey of Iran Abstracts.

Samani, B., 1993. Saghand formation, a riftogenic unit of upper Precambrian in Central Iran. Scientific Quart. J. Geol. Surv. Iran 2, 32–45 (In Farsi with English abstract).

Şengör, A.M.C., 1990. A new model for the late Palaeozoic-Mesozoic tectonic evolution of Iran and implications for Oman. In: Robertson, A.H.F., Searle, M.P., Ries, A.C. (Eds.), The geology and Tectonics of the Oman Region. Geological Society London Special Publications, pp. 797–831.

Sillitoe, R.H., Burrows, D.R., 2002. New field evidence bearing on the origin of the El Laco magnetite deposit, northern Chile. Econ. Geol. 97, 1101–1109.

Simon, A.C., Pettke, T., Candela, P.A., Piccoli, P.M., Heinrich, A.H., 2004. Magnetite solubility and iron transport in magmatic-hydrothermal environments. Geochim. Cosmochim. Acta 68, 4905–4914. https://doi.org/10.1016/j.gca.2004.05.033.

Stosch, H.-G., Romer, R.L., Daliran, F., Rhede, D., 2011. Uranium-lead ages of apatite from iron oxide ores of the Bafq District. East-Central Iran. Miner. Depos. 46, 9–21.

https://doi.org/10.1007/s00126-010-0309-4.

Sun, S.-S., McDonough, W.F., 1989. Chemical and isotopic systematics of oceanic basalts: implications for mantle composition and processes. Geological Society London Special Publications, pp. 313–345.

Taghipour, S., Kananian, A., Somarin, A.K., 2013. Mineral chemistry and alteration parageneses of the Chogart iron oxide- apatite occurrence, Bafq district, Central Iran. Neues Jahrbuch für Geologie und Paläontologie 269, 221–240. https://doi.org/10.1127/0077-7749/2013/0346.

Taghipour, S., Kananian, A., Harlov, D., Oberhänsli, R., 2015. Kiruna-type iron oxide apatite deposits, Bafq district, Central Iran: fluid-aided genesis of fluorapatite monazite-xenotime. Can. Miner. 53, 479–496.

Takin, M., 1972. Iranian geology and continental drift in the Middle East. Nature 235, 147–150.

Taylor, R.P., Feyer, B.J., 1983. Rare earth element geochemistry of granitoid mineral deposits. Canad. Inst. Min. Metal. Bull. 76, 74–84.

Torab, F.M., 2008. Geochemistry and Metallogeny of Magnetite Apatite Deposits of the Bafq Mining District, Central Iran. Doctoral thesis. Clausthal University of Technology, Germany.

Torab, F.M., Lehmann, B., 2007. Magnetite-apatite deposits of the Bafq district, Central Iran: apatite geochemistry and monazite geochronology. Mineral. Mag. 71, 347–363. https://doi.org/10.1180/minmag.2007.071.3.347.

Tornos, F., Velasco, F., Hanchar, J., 2017. The magmatic to magmatic-hydrothermal evolution of the El Laco Deposit (Chile) and its implications for the genesis of magnetite-apatite deposits. Econ. Geol. 112 (1595), 1628.

Tornos, F., Velasco, F., Hanchar, J., 2016. Iron-rich melts, magmatic, magnetite, and superheated magmatic-hydrothermal systems: the El Laco deposit. Chem. Geol. 44, 427–430.

Tornos, F., Velasco, F., Morata, D., Barra, F., Rojo, M., 2011. The magmatic hydrothermal evolution of the El Laco deposit as tracked by melt inclusions and isotope data. In: SGA Biennial Meeting, Let's Talk Ore Deposits, Proceedings, pp. 443–445.

Veksler, I.V., Dorfman, A.M., Borisov, A.A., Wirth, R., Dingwell, D.B., 2007. Liquid immiscibility and the evolution of basaltic magma. J. Petrol. 48 (11), 2187–2210.

Velasco, F., Tornos, F., Hanchar, J., 2016. Immiscible iron- and silica-rich melts and magnetite geochemistry at the El Laco volcano (northern Chile): evidence for a magmatic origin for the magnetite deposits. Ore Geol. Rev. 79, 346–366.

Waychunas, G.A., 1991. Crystal chemistry of oxides and oxyhydroxides. In: Lindsley, D.H. (Ed.), Oxide Minerals: Petrologic and Magnetic Significance. Reviews in Mineralogy, pp. 11–61.

White, A.F., Peterson, M.L., Hochella, M.F., 1994. Electrochemistry and dissolution kinetics of magnetite and ilmenite. Geochim. Cosmochim. Acta 58, 1859–1875.

Williams, P.J., Barton, M.D., Johnson, D.N., Fontboté, L., De Haller, A., Mark, G., Oliver, N.H.S., Marschik, R., 2005. Iron oxide-copper gold deposits. In: Geology, space-time distribution, and possible modes of origin. In: Hedenquist, W., Thompson, J.F.H., Goldfarb, R.J., Richards, J.P. (Eds.), Economic Geology 100th Anniversary Volume. Society of Economic Geologists, pp. 371–405.

Wilson, B., 1989. Igneous Petrogenesis a Global Tectonic Approach. Unwin Hyman, London.

Wood, B.J., Nell, J., Woodland, A.B., 1991. Macroscopic and microscopic thermodynamic properties of oxides. In: Lindsley, D.H. (Ed.), Minerals: Petrologic and Magnetic Significance. Reviews in Mineralogy. Mineralogical Society of America, pp. 265–302.

Zhou, M.F., Robinson, P.T., Lesher, C.M., Keays, R.R., Zhang, C.J., Malpas, J., 2005. Geochemistry, petrogenesis and metallogenesis of the Panzhihua gabbroic layered intrusion and associated Fe-Ti-V oxide deposits, Sichuan province, SW China. J. Petrol. 46, 2253–2280.